Nanoscale Advances

ROYAL SOCIETY OF CHEMISTRY

REVIEW

View Article Online
View Journal | View Issue

Cite this: *Nanoscale Adv.*, 2021, **3**, 73

Micro/nanostructured gas sensors: the physics behind the nanostructure growth, sensing and selectivity mechanisms

N. K. Chowdhury and B. Bhowmik *

Micro/nano sensors based on oxide semiconductors have received much interest worldwide due to their remarkable electrical conductivity, good stability, wide range of dimensional structures, large-scale production potential, and cost effectiveness. The present review extensively investigates the physics behind the nanostructure growth, gas sensing, and selectivity mechanisms of different micro/nano-based devices. Mainly, planar, vertical, heterojunction, and thin film devices are discussed along with their pros and cons in relation to gas sensing and transport mechanisms. The sensing behaviours of such devices have been explained considering nanostructure morphology (particles and pore sizes), surface states (type of defect states and defect concentrations), and interfaces (intra- and inter-grain boundaries). Further, nanostructures with different dimensions, such as nanoparticles, nanowires, nanorods, nanoplates/nanosheets, nanotubes, hollow spheres, and nanoflowers, have also been taken under consideration.

Received 13th July 2020
Accepted 22nd October 2020

DOI: 10.1039/d0na00552e

rsc.li/nanoscale-advances

Introduction

Micro/nano sensors are essential for detecting toxic polluting gases for controlling vehicle and industrial emissions, ensuring home security, and allowing environmental monitoring.[1] Gas sensing technology based on surface acoustic wave (SAW), quartz micro-balance (QMB), gas chromatography mass spectrometry (GC-MS) and chemiresistors has received much attention in the last decade.[2] Among these, metal oxide chemiresistive sensors (MOXChem) are mostly used in domestic, commercial, and industrial settings, due to their lower fabrication costs, ease of production, and compact size.[1,2] In recent years, air pollution has become a major concern around the globe.[3] The majority of air pollution is caused by toxic chemical and compounds involving NH_3, O_3, CO, CH_4, *etc.*[4] The location-specific detection of VOC molecules, especially those due to leakage, can possibly be used to control the pollution threat from chemical/drug industries and home appliances. Harmful pollutants based on oxide forms of nitrogen (like NO, NO_2, and NO_x), oxides of carbon (CO, CO_2), ozone (O_3), and suspended liquid particles in the atmosphere (many VOCs, such as methanol (CH_3OH), ethanol (C_2H_5OH), acetone (CH_3COCH_3), benzene (C_6H_6), and toluene ($C_6H_5CH_3$)) are responsible for harsh effects.[5–8]

The performance of oxide-based sensors is controlled by their morphologies and structures. Improvements in sensor parameters, such as increasing the sensitivity, selectivity, and speed of reaction, through variations in nanostructure dimensionality have been a prime focus in recent years.[3,4,10] For example, to achieve better selectivity for a particular species while employing oxide-based nanostructured sensors, some previously adopted strategies have been: (i) the incorporation of foreign elements, (ii) the use of hybrid composite materials as sensing materials, (iii) the variation of the sensor operating temperature, (iv) functionalization with noble metals as surface modifiers, and (v) the use of electronic nose/multi-sensor arrays examining gas fingerprints.[1–10] The generic definitions of the different dimensional structures in the nanoscale regime are as follows: (i) when all three spatial dimensions (*X*, *Y* and *Z*) are in the nanometer range, this is known as 0D (zero-dimensional), *e.g.* nanoparticles and nanoclusters; (ii) when any two dimensions (either *XY*, *YZ*, or *ZX*) are in the nanometer range, *e.g.* nanotubes, nanorods, and nanowires, this is known as 1D (one-dimensional), (iii) when only one spatial dimension (either *X*, *Y*, or *Z*) is nanometric, such as in thin films or nanosheets, this is known as 2D (two-dimensional); and (iv) when there is a combination of 0D, 1D, and 2D elements in close proximity to form interfaces having all three dimensions, for example compact polycrystals with nanosized grains or 3D porous nanostructures, this is known as 3D (three-dimensional).[11–13]

The controlled growth of oxide nanostructures

High-quality nanostructures synthesized through feasible methods, such as sputtering, sol–gel and hydrothermal synthesis, spray coating, chemical vapor deposition (CVD), *etc.*, with uniform sizes are widely used for different

Thin Film Devices Laboratory, National Institute of Technology, Jamshedpur, India. E-mail: bb.cemk.ece@gmail.com

applications.[14–23] Among the different synthesis methods, the hydrothermal process has the advantages of simplicity, good morphological control, low cost, and good long-term stability for the preparation of Ce-doped In_2O_3 nanomaterials.[24] Solvothermal synthesis is another suitable method and it has been used for the synthesis of porous $ZnFe_2O_4$ nanospheres with the aid of heat treatment. Investigations revealed that gas sensors using this material showed improved selectivity for acetone at 200 °C.[25] It was observed that solution-based approaches are more beneficial than physical processes for high-quality nanostructure preparation due to the facile and economic synthesis, large-scale production, and low reaction temperatures.[14] However, the issue of nanostructure deformation during high-annealing-temperature treatment for the purpose of crystallization necessitates research into alternative sophisticated approaches.[15] For example, vapor/liquid phase methods have been mostly adopted for 0D-nanoparticle or quantum-dot preparation, with specific exposed facets for gas sensing applications.[10] Specific facets have different reaction kinetics toward different gases and, therefore, one can easily fabricate selective gas sensors based on materials with the growth of particular exposed facets. In this regard, template-based methods (soft or hard templates) based on organic or inorganic precursors have widely been accepted for fabricating mesoporous or hollow metal-oxide nanostructures.[15]

Continuous pores with tunable size can easily be realized *via* this method. Most template-based approaches for oxide nanostructure preparation use PEO_{20}–PPO_{70}–PEO_{20} (P_{123}), PEO_{106}–PPO_{70}–PEO_{106} (F_{127}), and poly(ethylene-*co*-butylene)-*block*-poly(ethylene oxide) (KLE) as templates.[15] The agent KLE helps to control synthesis processes, with the required micelle size, which depends on the block length, and a high decomposition temperature.[26] KLE increases the stability at high temperature (600 °C). Zhou *et al.* investigated a direct synthetic strategy for mesoporous ZSM-5 zeolites *via* employing block copolymer templates like P_{123} and F_{127}. It has been observed that when a gel-to-zeolite transformation happens, the Pluronic templates worked as a platform in order to maintain the spacing.[27] Hard templates are used relatively less often because of etching problems. Representative hard templates, like poly(methyl methacrylate) (PMMA) spheres, silica spheres, and polystyrene (PS) spheres, have been used to obtain macroporous and mesoporous structures.[3] After nanostructure formation, the outer template structure is removed either through annealing in ambient air or etching with NaOH (for SiO_2 spheres) or CH_2Cl_2 (for PS spheres).[3]

Cutting-edge nanotechnology does not guarantee the compactness of nanodevices involving integrated circuits. However, it can guarantee the synthesis of highly ordered nanomaterials through accurate position control over a large surface area in an integrated circuit. In this regard, vertical stacking, self-assembly, or rubbing techniques may be used for precise alignment in a short time-span to realize highly integrated devices. Most nanoparticle suspension solutions have been uniformly distributed over layers by means of spray-coating or spin-coating techniques.[15,16] However, when using such methods, the locations of the nanoparticles/microparticles are in question, as it is unclear how precisely they can be aligned. Sometimes, external temperature can be used to align the particle positions in a layer structure. A recent study found that polydimethylsiloxane (PDMS) can be used as a good aligner for microparticle positioning.[8] The use of PDMS in association with rubbing techniques ensures precise particle positioning without any solvent and in a very short time span. Sensitivity can be enhanced to some degree in the case of materials prepared *via* a self-assembly process. Self-assembly-prepared SnO_2 nanowires showed superior hydrogen detection abilities.[1] An engineering approach that makes nanomaterials *via* self-assembly changes the surface states, which can effectively disrupt the intrinsic properties of a material and possibly enhance the gas-sensing performance compared to ultrasonically dispersed nanomaterials in ethanol.[1]

Generally, sputtering techniques are found to be the most promising methods for synthesizing p-type (Cr_2O_3, NiO, and CuO) ultrathin nanowire (thickness: ~14 nm) arrays with a grain size of ~5 nm (as shown in Fig. 1(b–d)).[2] Ar^+ ion bombardment and the presence of different transition metals (Cr, Ni, and Cu) in the sputtering chamber can easily result in the fabrication of different types of Cr_2O_3, NiO, and CuO nanowire arrays. The purpose of Ar^+ ion bombardment is to control the etching of the transition metal to form oxide nanowires with different feature dimensions based on the etching rate. A study by Cho *et al.* revealed that a lower Ar^+ ion bombardment etching rate with Cr metal results in shorter Cr_2O_3 nanowires with a height of ~100–200 nm, whereas a higher etching rate with Cu and Ni produces nanowires with a height > 300 nm.[2] Sputtering techniques offer better control over film thickness, with precise layer uniformity and good channel connectivity.[3] Even better nanostructure uniformity may be achieved through atomic layer deposition (ALD).[16] One of the most important benefits one can expect from ALD growth is the precise control of thickness at the atomic level. Sub-nanometer thickness control of oxide materials was achieved through the sequential use of self-limiting chemical reactions.[16] In the ALD process, thin-film growth started with the nucleation of metal nanoparticles on the substrate surface. However, it is worth mentioning that a surface energy difference between the deposited material and the substrate leads to discontinuities in film growth. Therefore, to obtain film continuity, one should carry out repeat chemical reaction cycles on the surface.

The nucleation and growth of homogeneous materials do not create many problems during sensor development. However, difficulties arise when assembling heterogeneous nanomaterials during sensor design and functional integration with microelectronic circuitry. The synthesis of heterogeneous structures, like CuO nanospikes, TiO_2 nanotubes, and ZnO nanowires, on the same platform (substrate) possibly offers the development of an array of sensors for the screening of gases from mixtures of multiple gases.[17] Therefore, one would not have to develop separate selective sensors for different gases. However, as already mentioned, gas-specific multi-sensor design on the same substrate was ruled out in an earlier effort due to poor contact between the electrode and sensing materials, poor controllability, and lower throughputs.[17]

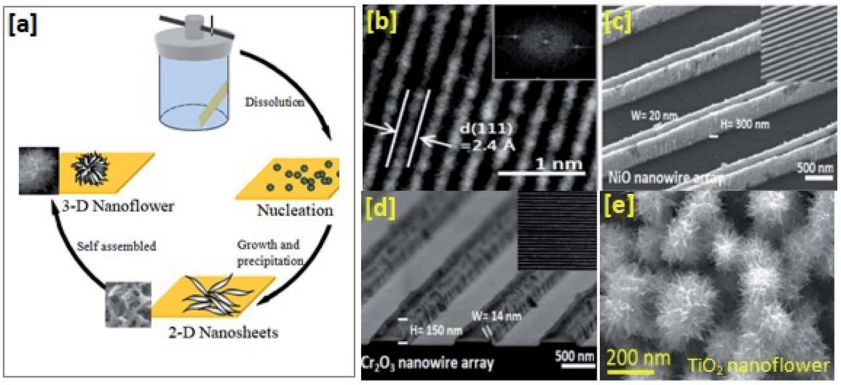

Fig. 1 (a) The nucleation, precipitation, and growth of 2D nanosheet ensemble 3D spheres. (b) A TEM image of CuO revealing lattice spacing of 2.4 Å. (c) An FESEM image of a NiO nanowire array. (d) An FESEM image of Cr_2O_3 arrays (this figure has been reproduced from ref. 2 with permission from ACS Publications, copyright 2016). (e) An FESEM image of TiO_2 nanoflowers (this figure has been reproduced from ref. 20 with permission from IEEE Transactions on Nanotechnology, copyright 2017).

Heterogeneous nanostructure-based multi-sensors synthesized *via* employing a hybrid combination of focused ion beam, hydrothermal, and liquid-phase deposition (LPD) techniques, which realized localized liquid-phase reactions through well-controlled thermal treatment, were found to offer a promising solution, mitigating the associated problems related to fabricating multiple sensors on the same platform.[17]

Obtaining ZnO nanoparticles with various shapes may be possible when employing zinc acetate as the metal precursor. Aggregated nanoparticles could possibly be converted to different shapes depending on the applied ultrasound energy.[18] The ultrasonication of the nanoparticles for 15 min resulted in ZnO nanorods (having a diameter of 50 nm), whereas prolongation to 30 min produced 3D nanoflowers. Most solution-based ZnO-nanostructure growth happens in one dimensional direction due to the unique hexagonal crystal structure.[14] Further, directing/capping agents play a major role in realizing different shapes and sizes of nanostructures. Directing/capping agents accelerate growth at certain faces *via* blocking some other faces of the crystal structure.[19] Some commonly used capping agents for one-dimensional nanostructure growth are HCl, NaCl, $H_2C_2O_4$, Na_2SO_4, and Li_2SO_4.[10] It is believed that the governing factors determining the final crystal phase and nanostructure morphology are related to stabilizing cations (*e.g.* Na^+, NH_4^+, Li^+, *etc.*) and directing anions (*e.g.* SO_4^{2-}, Cl^-, $C_2O_4^{2-}$, *etc*).[10] ZnO nanomaterials obtained *via* solution-based techniques offer polar as well as non-polar faces. However, most of the nucleation growth occurs at the polar faces. Growth initiated through the aggregation of ZnO nuclei towards polar faces (the axial direction) ultimately produces 1D nanostructures. On the other hand, nucleation towards non-polar faces (the equatorial direction) results in tabular nanostructures, such as nanoplates, nanosheets, *etc.* Growth at non-polar faces happens only when the passivation of polar faces is carried out *via* a growth modifier (suppressing growth in the axial direction).

Sol–gel derived TiO_2 nanoflower synthesis occurs as follows (shown in Fig. 1(a) and (e)): titanium tetraisopropoxide, $Ti(OPr)_4$, is the initial precursor, with anhydrous ethyl alcohol, deionized water, and HCl used as other chemicals.[21] Deionised water, HCl, and ethyl alcohol were mixed and stirred vigorously. Then 0.4 M titanium tetraisopropoxide, $Ti(OPr)_4$, was mixed gradually into the mixture for the hydrolysis of the precursor. The role of HCl is to control the condensation rate so that fast gelation can be prevented. The entire transparent mixture is then kept at room temperature for 30 days. Similarly, the substrate-dependent formation of different nanostructures has been observed.[3,4,14] The hydrothermal synthesis of ZnO thin films produces hexagonal nanorods (~200 nm in diameter) when the substrate is alumina ceramic tubes without Al nanolayers.[12] On the other hand, the addition of Al nanolayers onto the alumina ceramic tubes resulted in ultrathin ZnO nanosheets (thickness: ~15 nm).[12] Nanostructures with numerous pores have received significant interest due to their unique gas sensing properties. Sensitivity improvement through pore-size control is possibly a similar powerful method to grain-size variation. Electrochemical anodization or an etching process produces a porous structure. Increasing the anodization voltage of Ti foil offers pores with longer lengths (etching towards the bulk material), whereas variations in the electrolyte concentration resulted in variations in the pore diameter.[22] Zn-doped NiO crystals were synthesized *via* an electrolytic approach, and it was found that the process is advantageous due to excellent reproducibility, reversibility, stability, and selectivity toward NH_3.[28] The synthesis process for porous $ZnFe_2O_4$ nanospheres is as follows: 1 mmol of zinc nitrate hexahydrate ($Zn(NO_3)_2 \cdot 6H_2O$) and 2 mmol of ferric nitrate nonahydrate ($Fe(NO_3)_3 \cdot 9H_2O$) were dissolved into 40 mL of ethanol–ethylene glycol mixed solution. After stirring for a while, the solution was heated at 180 °C for 24 h and then left to cool down. Further, the remaining precipitate was collected and washed with deionized water and ethanol repeatedly and dried at 80 °C for 12 h. Lastly, the dried precipitate was heated at 400 °C for 2 h and porous $ZnFe_2O_4$ nanospheres were obtained.[25]

The hydrothermal synthesis of pure SnO_2 showed randomly directed nanorods. Doping with foreign elements may or may not

affect the nanostructure dimensionality, depending on the type of precursor available in solution. As evident in ref. 11, it is possible that the existence of Na^+ cations from NaOH helps to retain the shape of the nanorods. However, the size of the nanorods is decreased and they are transformed to closely packed flower-like bunches (diameter: $\sim 3 \pm 1$ μm) upon the addition of Ni particles to solution.[13] Precise morphology evaluations further confirm the nanosheet-like (thickness: ~20 nm) petal structures of the nanoflowers, with well-defined lattice fringes; the (110) and (101) lattice planes show distances of 0.337 nm and 0.265 nm, respectively.[11] Similarly In_2O_3 porous nanospheres with Ce dopant were synthesized *via* employing a low-cost simple hydrothermal process. 5 mmol of $InCl_3 \cdot 4H_2O$ and 15 mmol of citric acid were dissolved in 65 mL of deionized water, and 30 mmol of urea was added into the solution. Later, $Ce(NO_3)_3 \cdot 6H_2O$ was also added. The resultant mixed solution was then treated at 130 °C for 12 h and cooled to room temperature.[24]

Surface and bulk properties of oxide materials

Most metal oxide materials have various geometries and electronic configurations with semiconducting nature.[5,7,10,17] Oxides are most often utilized in the manufacture of microelectronic circuits, sensors, piezoelectric gadgets, power modules, coatings for surface passivation, *etc.*[29] Apart from nanostructuring effects, the optical, chemical, transport, and electronic properties of oxides further influence sensor performance.[15] The elementary optical properties of oxides can be experimentally obtained based on reflectivity and absorption measurements. It was observed that the transport properties are mainly governed by the ionic or mixed-ionic movement, or the electronic conductivity of the oxide material. The oxide ionic movement and electronic conductivity were found to be better in solid nanostructure form.[29] In addition, oxidation–reduction reactions in the context of absorption and desorption are also found to be more favorable. Most oxide materials possess highly reactive electronic transitions, wide band gaps (3–5 eV), high dielectric constants, and good electrical characteristics.[10–17,22] For instance, the large binding energy of ~60 meV, excellent thermal and chemical stability, large band gap of 3.37 eV, and high electron mobility are added advantages of ZnO when it is used as a sensing material.[29] Another extremely important characteristic of ZnO is the crystal interplanar spacing, which is found to be 0.518 nm and corresponds to the (0001) plane of wurtzite ZnO; in SnO_2, the (101) plane of rutile SnO_2 is reported to have crystal interplanar spacing of 0.26 nm.[19]

Metal oxides exhibit various electrophysical features, ranging from acting as insulators to wide band-gap semiconductors.[2] Oxide materials offer ionic or mixed-ionic and electronic conductivity. Based on Boltzmann statistics, the amount of electronic charge in a metal oxide is a function of the band gap energy.[30] These properties of different oxide materials facilitate faster electron transfer through grain boundaries, resulting in fast response and recovery times in sensors.[3,10] Response and recovery times vary greatly in sensors made with different types of materials. The influence of adsorption and desorption kinetics is responsible for the dissimilar response and recovery characteristics of different materials. Porous materials offer easy diffusion, but complete desorption from the inner core and from intertubular voids takes a longer time. That's why in a porous material, the response time is faster than the recovery time.[22] On the other hand, in a dense material, the penetration of gaseous molecules is limited to a few nanometers, resulting in faster recovery characteristics at the cost of a slower response time. For example, 2D ordered macroporous TiO_2 nanostructures have nanoarchitectures that offer a high and rapid response.[31] Similarly, 2D ordered macroporous SnO_2 film with a MEMS-based sensing chip exhibited a high and fast response to ethanol.[32] Metal oxides can be categorized as transition-metal oxides (Fe_2O_3, NiO, Cr_2O_3, *etc.*) or non-transition metal oxides. Further, non-transition metal oxides can be categorized as pre-transition metal oxides (Al_2O_3) and post-transition metal oxides (ZnO, SnO_2), which have, in general, one oxidation state and require higher energies to make transitions to other oxidation states.[4,23] Their structural instability, lower electrical conductivity, and inability to produce electron–hole pairs make them less preferable for gas sensor applications.[23] To the contrary, a higher rate of chemisorption and the subsequent accumulation of electrons/holes are attractive and preferred for the design of gas sensors. For example, a transition-metal oxide like TiO_2 offers wide energy band-gaps of 3.0 eV, 3.2 eV, and 3.14–3.40 eV in its rutile, anatase, and brookite phases, respectively.[33–37] However, its surface properties can be further improved *via* adding noble metals like Ag, Au, Pd, and Pt to increase the number of reaction centres and reduce the activation energy required for the oxidation and reduction of target species.[38]

The band gap engineering of nanostructured materials is possible *via* adding structural defects or doping with non-metal and metal elements.[33] Transition-metal oxide materials offer high refractive indices. For example, TiO_2 has a refractive index of 2.71 in rutile form, 2.53 in anatase form, and 2.64 in brookite form.[33–37] Oxide materials offer high dielectric constants (ε_{TiO_2} = 40 to 86) and high resistivities (extending to 10^8 Ω cm).[33–37] As far as gas sensing is concerned, the surface properties are more important than the bulk counterparts. However, the properties of the bulk will ensure the robustness and stability of the system. Bulk properties can be characterized based on the crystallographic structure of the oxide.[37] Polycrystalline oxide materials are more preferred than single crystal oxide materials for gas sensing.[10,23,37] Polycrystalline oxides offer higher responses, whereas single crystals ensure sensor stability. One can easily correlate the sensor parameters with the crystal properties. For example, the anatase crystalline phase of TiO_2 (as shown in Fig. 2(b)) is more reactive towards gas than the rutile crystal (shown in Fig. 2(a)), whereas brookite is insensitive to gases.[33–39] Brookite and rutile crystals are more stable phases, even at higher temperature. Therefore, a trade-off between sensor response and stability necessitates the choice of a crystallographic phase based on the sensor applications.

Sensor parameters and associated devices

The general correlation between sensor parameters has been investigated in a qualitative as well as quantitative manner. The

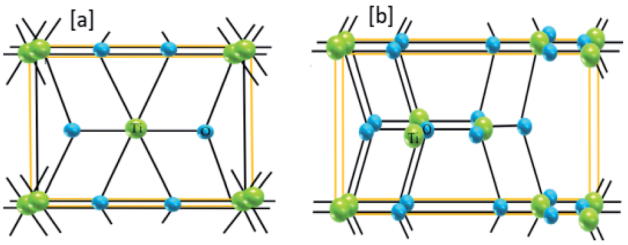

Fig. 2 The bulk crystalline structures of (a) rutile-phase and (b) anatase-phase materials; green: titanium, blue: oxygen (this figure has been redrawn from ref. 4).

performances of oxide-based sensors are governed by the morphologies and structures of the sensing materials. For example, adjusting the particle size of the sensing material or doping with foreign elements can result in a great improvement in the sensor response. Based on the "small size effect" phenomenon, the response (S) increases when the particle size (d) of the material is approximately double the thickness of the space-charge layer (w).[29] Nanomaterials offers a greater surface to volume ratio (SVR) depending on the dimensions of the nanostructures. A higher SVR leads to more adsorption sites, facilitating a higher sensor response (S). On the other hand, the thickness of the grown film (t) or the particle size (d) is inversely proportional to the sensitivity (S). This relationship ($S \propto 1/d$) can lead to a faster response time.[23] In addition, the temperature has a significant influence on the sensor response time and reversibility. A higher operating temperature drastically speeds up the response time and improves the reversible characteristics of a sensor. However, a higher operating temperature sometimes limits maximum detection owing to the tendency of adsorbed molecules to saturate on the surfaces.[4] The problem of the need for high operating temperatures can be easily resolved through the modification of structural parameters like crystal shape and orientation.[4] The manipulation of materials on the nanoscale with reactive crystal facets can be an alternative approach for reducing operating temperatures and, hence, supporting low power consumption.[4] The effects of pore size on sensitivity have been explored by many researchers.[22] Porous sensing materials can offer enhanced sensitivity in a linear fashion.[23] However, the pore size does not always maintain a linear relationship with sensitivity. Furthermore, the response/recovery rates become faster in materials with numerous pores. In a porous material, the gas diffusion mechanism solely depends on the size of the pores and the gas diffusion constant.[7] Based on the Knudsen diffusion process, the diffusion constant (D_K) can be empirically related to the pore radius (r), temperature (T), molecular weight (M), and gas constant (R) based on the relationship $D_K = 4r/3(\sqrt{2RT/\pi M})$.[7] The diffusion constant proportionally varies with the pore radius, which can lead to higher sensitivity. As far as crystallinity is concerned, materials with smaller crystallites exhibit greater sensitivity though an increase in the depletion layer width (w).[7] The depletion layer width (w) is related to the sensor response as follows: $S = (\Delta n/n) \times w$, where n is the charge carrier (e/h) concentration and Δn is the difference in charge carrier concentration in air and after gas exposure. The depletion layer width (w) can be further correlated with temperature as follows: $w = (\varepsilon_o kT/ne^2)^{0.5}$, where ε_0 is the dielectric constant of the material, k is the Boltzmann constant, and T is temperature.[19]

Sensing mechanisms

The working principle of a gas sensor is based on changes in the electrical conductivity of the sensing material. Due to the enormous number of surface sites, most target gas molecules are adsorbed by oxygen ions that have been already adsorbed at the metal-oxide surface. Interactions between the adsorbed target species and the oxygen ions can modulate the charge carrier concentration and hence change the conductivity (or resistivity) of the material. Table 1 shows a summary of the conductivity changes of n-type and p-type materials upon exposure to reducing and oxidizing gases.

Generally, physisorption and chemisorption are the two processes that take place at the sensing layer, depending on temperature variations. Physisorption is an exothermic reaction that occurs at low temperature and chemisorption is an endothermic reaction that occurs at higher temperatures.[2] In general, the physisorption of adsorbed O_2 and its subsequent transformation to O_2^- happen at lower operating temperatures (<100 °C).[2,19] On the other hand, at relatively higher temperatures (>100 °C), physisorbed oxygen species are transformed into chemisorbed O^-, which is more stable and reactive to different types of gases.[40–42] Therefore, temperature has a significant role in this mechanism, as it ensures the formation of different oxygen species (as shown in eqn (1)–(3)).

$$O_{2(gas)} \leftrightarrow O_{2(ads)} \quad (1)$$

$$O_{2(ads)} + e^- = O_2^-[<100\ ^\circ C] \quad (2)$$

$$O_{2(ads)}^- + e^- = 2O_{(ads)}^-[100\text{–}300\ ^\circ C] \quad (3)$$

The width of the depletion layer during the aforementioned phenomenon is found to be at a maximum provided the oxide semiconductor is n-type. However, the width of the depletion layer might be modulated depending on the type of target species that interacts with the oxygen species.[41] For example, an n-type sensing material exposed to oxidizing gases (NO, NO_2, Cl_2, and O_3) results in a depletion layer with a larger width compared to the case when only oxygen was adsorbed on the sensing surface.[23,41] Such gas-dependent depletion layer thickness variations lead to modulations of electron concentrations, eventually changing the resistance of the sensing material.

Table 1 A summary of the conductivity changes of n-type and p-type materials in reducing and oxidizing gases

Material property	n-Type	p-Type	Type of gas
Conductivity	Increases	Decreases	Reducing
Carrier concentration	Increases	Decreases	
Conductivity	Decreases	Increases	Oxidizing
Carrier concentration	Decreases	Increases	

The role of junction effects

For a better understanding of sensing phenomena, a SnO_2 nanowire model exposed to an oxidizing gas (NO_2) has been taken under consideration (as shown in Fig. 3(a) and (b)).[40] Under ambient conditions, the electron-donating capabilities of SnO_2 depend on the state of the oxygen vacancies (V_O), which is largely governed by the secondary ionization energy.[8] The release of electrons and a subsequent change to a +1 ionic valence state lead to a change in the depletion width (w).[8] Upon the exposure to NO_2 (an oxidizing gas) of the nanowire junctions, two ionic states below the edge of the conduction band are formed.[8] Such ionic states cause the depletion layer to increase in width and, hence, undergo band bending, compared to in the case of air exposure alone. These junctions correspond to active points where electrons from the conduction band of the semiconductor are transferred to the adsorbed NO_2 (acting as an electron acceptor), leading to the formation of a depletion layer near the junction and an increase in the potential barrier (as shown in Fig. 3(b)). A comparison between single nanowire devices (where only a single nanowire lies between two electrodes) and a multi-nanowire network reveals a more effective sensor response in the case of the latter due to the adsorption effects of multiple junctions.[40] To the contrary, a single nanowire device offers a fast response towards the target species, possibly attributed to the idea that electrons have almost no barrier (except the ohmic junction at the electrode-semiconductor interface) to overcome, whereas there are multiple barriers (formed between many nanowires) in the multi-nanowire network. Electron transport in the semiconductor is affected by the height of the potential barrier (Ψ_b). A potential barrier in micro/nano sensor devices may form either at the junction between two grains, at the electrode–semiconductor interface, or at both interfaces. However, the barrier height at the electrode-semiconductor (sensing material) interface (Ψ_{MS}) plays a significant role in determining the gas sensor performance. The electron flow does not face much of an obstacle to overcome the low barrier height at the ohmic junction (which forms at the electrode–semiconductor interface). However, in the case of Schottky contact, the barrier height (Ψ_{MS}) is related to the electron affinity (χ) and work function of the metal (Φ_m) as follows: $\Psi_{MS} = \Phi_m - \chi$.[7,8,40] The effects of the Schottky barrier interface between single wall carbon nanotubes (SWCNTs) and ZnO ($\chi = 4.35$ eV) have been investigated by Kim *et al.*[8] The authors suggest that the improved NO_2 sensing performance can be attributed to the formation of a lower Schottky barrier height of ~0.67 eV with the use of SWCNTs as electrodes ($\Phi_m = 5.02$ eV).[8] Electrode variations also have an influence on sensor parameters, which may be explained *via* employing a thermionic emission model to analyze the Schottky barrier height. Different electrodes, such as Au and Pd, have been studied to measure the differences in sensor response.[8] Obviously, work function differences between the two material will create a barrier height as follows: $\Psi_b = \Psi_{MS} = \Phi_m - \Phi_s = (k_B T/e) \times \ln(I_m/I_S)$, where Φ_s is the work function of the semiconductor, k_B is the Boltzmann constant, I_m is the current running through the metal, and I_S is the current running through the semiconductor. Therefore, based on the barrier height model, one can easily calculate the sensor response following the equation:[19]

$$\text{Response} = \exp\left(\frac{-e\Delta\Psi_b}{kT}\right) \quad (4)$$

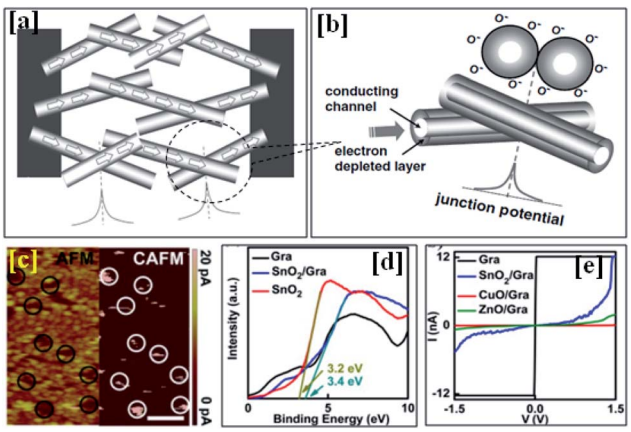

Fig. 3 (a) A schematic diagram showing a model of SnO_2 nanowires connected between two electrodes. (b) An enlarged view of nano-junction formation and a corresponding energy band diagram (this figure has been reproduced from ref. 40 with permission from IOP Publishing Ltd, copyright 2008). (c) CAFM current mapping of an oxide/graphene composite with a scanning area of 500 nm × 250 nm. (d) The XPS study of pristine graphene, an oxide/graphene composite, and an oxide material, and (e) the current voltage characteristics from the junction study (this figure has been reproduced from ref. 7 with permission from the Royal Society Of Chemistry, copyright 2015).

Carrier transportation through the geometry of a SnO_2/graphene junction has been studied using conductive atomic force microscopy (CAFM) (as shown in Fig. 3(c)).[7] One can understand the barrier height concept in the SnO_2/graphene junction by looking at Fig. 3(c) (the left side reveals an AFM image of the SnO_2/graphene surface, whereas the right side demonstrates the conductivity differences on the surface). The highlighted black circles represent void regions on the surface, which facilitate the flow of a larger amount of majority carriers (larger current), reflecting the existence of a smaller barrier height. Currents through the junction were measured at different bias voltages in CAFM mode for pristine graphene, SnO_2/graphene, NiO/graphene, and CuO/graphene (as shown in Fig. 3(e)). Fig. 3(e) suggests that a maximum current was recorded for the junction having the lowest barrier height. In this regard, SnO_2/graphene offered the lowest barrier height, as it has the maximum flow of carriers out of all the samples at the same bias voltage. Differences in barrier height can be confirmed through valance band spectra studies.[7] Valence band spectra from XPS data provide the electronic states near the Fermi level. For example, the differences between the valence band maximum and the Fermi level before and after SnO_2 deposition on graphene were found to be 3.2 eV and 3.4 eV, respectively (as shown in Fig. 3(d)). Therefore, electrons can pass through the SnO_2/graphene barrier height of 0.2 eV efficiently.

Zhang *et al.* investigated the performance of an acetone gas sensor made of heterostructured n-type SnO_2 with p-type reduced graphene oxide.[43] The gas interacts at the junction (the depletion layer), where acetone acts as an electron donor, thereby increasing the carrying of negative charge to the n-type thin-film. When acetone is absorbed, gas molecules cause a change in the hole concentration of RGO. As a result, the resistance of the sensor decreases. As far as the doping or addition of foreign elements is concerned, additional adsorption sites increase the sensor response drastically.

LUMO energy

The temperature-dependent gas sensing mechanism towards different gases (selectivity) can be further understood based on the concept of the lowest unoccupied molecular orbital (LUMO) energy model. The sensing of a particular gas can be related to the LUMO energy of the gas atom and the amount of gas adsorption on the sensing material at various working temperatures.[44] For example, a study by Wen *et al.*[44] suggested that the orbital energies of ethanol, methanol, acetone, and formaldehyde were found to be 0.12572 eV, 0.19728 eV, 0.20525 eV, and 0.21965 eV, respectively. Lower-LUMO-energy molecules can be detected at lower temperatures.[44] The study revealed that ethanol has the lowest LUMO energy (~0.12572 eV) and offers a maximum response at 280 °C. On the other hand, the molecules with higher LUMO energies (methanol, acetone, and formaldehyde) require higher operating temperatures (from 320–362 °C) to achieve a maximum response. This is possibly due to the inverse relationship between the electron transfer capabilities and the LUMO energy.

The role of defect states

The gas sensor response depends on the donor or acceptor type, semiconductor surface states, surface defects, native point defects, *etc.*[45] The relationship between the sensor response and defect states has been analyzed here considering a ZnO donor surface as a case study. Six types of defects are dominant in ZnO: zinc anti-sites (Zn_O), zinc interstitials (Zn_i), zinc vacancies (V_{Zn}), oxygen anti-sites (O_{Zn}), oxygen interstitials (O_i), and oxygen vacancies (V_O).[45] Owing to their higher formation energy, zinc anti-sites (Zn_O) are generally not found on the ZnO surface, whereas the relatively lower formation energies ensure an abundance of zinc interstitials (Zn_i) and oxygen vacancies (V_O). These defects (Zn_i and V_O) act as donors and offer electrons in the ZnO crystal structure. To the contrary, remaining defects, like zinc vacancies (V_{Ti}), oxygen interstitials (O_i), and oxygen anti-sites (O_{Ti}), accept free electrons and act as acceptors.[45] The electron accepting and donating mechanisms are shown in eqn (5) and (6).

$$V_O/Zn_i \rightarrow V'_O/Zn'_i + e^- (\text{electron donor}) \quad (5)$$

$$O_i/O_{Zn}/V_{Zn} + e^- \rightarrow O'_i/O'_{Zn}/V'_{Zn} (\text{electron acceptor}) \quad (6)$$

Oxygen adsorption and its transformation to O^- upon accepting one electron occur at the active sites of zinc interstitials (Zn_i) and oxygen vacancies (V_O) near the surface. These active sites act as oxidation centres for the target gas molecules. On the other hand, O_{Zn} and O_i reduce the formation of O^- species *via* accepting electrons and create an opposing effect during chemisorption compared to Zn_i and V_O.[37] Therefore, it can be stated that only specific defects having electron donation capabilities can enhance the sensor response dramatically. Generally, the sensor response initially increases at a faster rate and then the response rate decreases, gradually tending to a saturation level. Such a phenomenon can possibly be explained as follows: initial molecular adsorption at relatively lower energy binding sites expedites surface adsorption at a faster pace, resulting in a faster response, whereas the slow response is ascribed to the saturation of surface sites, with molecular interactions only occurring at the higher energy binding sites, *viz.*, defects, vacancies, and oxygen functional groups.[46] In addition, the greater the availability of high-energy binding sites at the sensing surface, the better the sensor recovery characteristics.

The role of humidity

It is essential to specify up to what percentage (%) level of humidity the sensor response remains invariable in a commercial sensor datasheet. Almost every micro/nano sensor possesses response variations in the presence of different levels of humidity. Therefore, in this section, humidity sensing mechanisms based on a proton (H^+) hopping model (as shown in Fig. 4) are discussed.[20] Water molecules on the sensing surface dissociate to form H^+ and OH^-. Dipole OH^- ions adsorb on the sensing surface and make bonds with the semiconductor grains. For a better understanding, we have considered TiO_2 as the semiconductor surface here. Mainly, dipole OH^- ions bonded with titanium interstitials, Ti_{Ti}, and formed water dipoles in the form of ($Ti^{\delta+}_{Ti}$– $OH^{\delta-}$), as shown in eqn (7) and (8). The bonding of OH groups with TiO_2 grain sites is shown pictorially in Fig. 4. On the other hand, H^+ ions (protons) hop from one grain to another through the temporary formation of hydronium ions (H_3O^+). Along the hopping path, ions (protons) may react with either adsorbed oxygen species (O^-) or lattice oxygen (O_O) based on the availability on the surface. Bonding

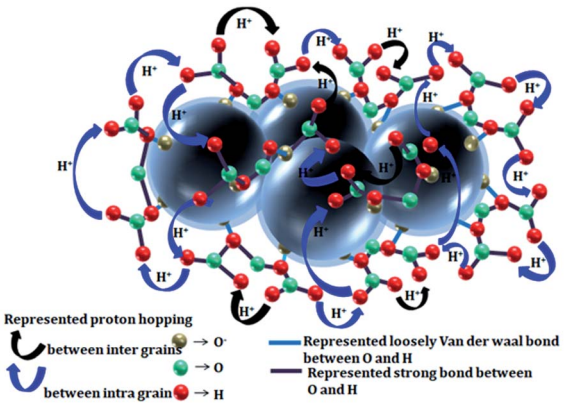

Fig. 4 Inter- and intra-grain proton-hopping model.

between H^+ and O^- produces neutral hydroxyl ions (OH) and many of these hydroxyls (OH) form water vapor, which is purged from the surface. To the contrary, the reaction of H^+ with lattice oxygen (O_O) offers either rooted (OH^+_{rooted}) or oxygen (V_O^{++}) vacancies *via* releasing electrons (as shown in eqn (7) and (8)). The process of water molecule adsorption can lead to H^+ transfer, which can not only change the electrical resistance but also the refractive index. The change in this latter property can be used to detect water vapor in the range between 10% and 90% relative humidity.

$$Ti_{Ti} + (H^+–OH^-)_{ads} + O_O = [Ti_{Ti}^{\delta+}–OH^{\delta-}] + OH^+_{rooted} + e^- \quad (7)$$

$$2Ti_{Ti} + (H^+–OH^-)_{ads} + O_O = 2[Ti_{Ti}^{\delta+}–OH^{\delta-}] + V_O^{++} + 2e^- \quad (8)$$

Influence of the sensor structure

Resistive sensors. The structure of a typical thin-film resistive sensor is shown in Fig. 5(a). It consists of gas-sensitive film deposited on an insulating substrate, like Si/SiO_2, ITO, polyimide, FTO, *etc.*[47] The sensitive film might be a porous semiconductor layer, like TiO_2, SnO_2, ZnO, and WO_3, or a composite material (Pd/SnO_2, RGO–TiO_2, Au–WO_3).[21,47,51–53] Two electrodes (Au, Pd, Pt, *etc.*) were deposited on top of the sensitive film to make ohmic contact. Heating elements (a micro-heater) were fabricated under the lower surface of the substrate to allow the temperature elevation that is required for obtaining a reasonable gas reaction rate (as shown in Fig. 5(d)).[47,50] TiO_2, as a sensing material in resistive mode, has been extensively used in automotive exhaust gas sensors. In these sensors, the concentration cell comprises an oxygen-ion conductor, which is used to measure the concentration of oxygen in the exhaust gas. Two types of electrode, *viz.*, a reference electrode and a sensing electrode, were used for the detection of differences in oxygen concentrations.[51] These sensors offer remarkable sensor responses to different VOCs but their limited selectivities and sluggish response and recovery times have forced researchers to look for alternative device structures.

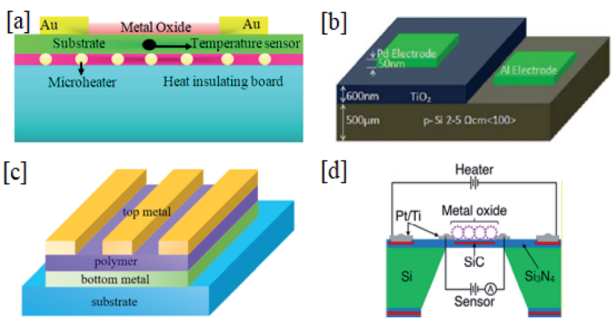

Fig. 5 Schematic diagrams of (a) a thin-film resistive gas sensor (this figure has been reproduced from ref. 47 with permission from Elsevier, copyright 2003), (b) a metal–insulator–semiconductor (MIS) structure, (c) a metal–insulator–metal (MIM) structure, and (d) a sensor with microheater integration (this figure has been reproduced from ref. 50 with permission from ACS Publications, copyright 2017).

MIS sensor devices. Lundström first investigated the metal–insulator–semiconductor (MIS) structure for improving the sensor response time through the vertical transport of majority carriers.[48] In such devices, a high response is accomplished through the use of a permeable semiconductor layer deposited on a semiconducting substrate.[54,55] A catalyzed top-gate electrode (Au, Pd, Pt, *etc.*) was deposited on the top surface of the permeable semiconductor layer and one bottom contact was placed at the interface of the sensing layer and the substrate, as shown in Fig. 5(b). Permeable layers are mostly used in MIS structures because of the porosity, which facilitates target gas molecules penetrating from the surface towards the bulk.[54–56] Further, the huge number of interfacial states and volume traps in the permeable layer produce a strong-field state; this eventually becomes the oxidation–reduction centre for target gas molecules. The higher number of gas interactions and ease of bond-breaking possibly are the reasons for the higher response and fast response/recovery profile.[40] However, these electrophysical characteristics of the MIS structure do not offer better gas sensitivity and selectivity during prolonged operation and/or storage times.[50] Concepts related to the MIS structure can be extended to the fabrication of metal–(insulator)–semiconductor (MS/MIS) Schottky diode sensors, metal–insulator–semiconductor (MIS) capacitor sensors, and metal-oxide–semiconductor field-effect transistor (MOSFET) sensor devices.

MIM sensor devices. The metal–insulator–metal (MIM) structure is almost similar to the MIS structure, except the bottom electrode is the connection to the substrate. MIM structures (Fig. 5(c)) as gas sensors have been the least investigated. The vertical electron transport mechanism of this structure offers fast response/recovery characteristics, but at the cost of a lower response magnitude.[57] Pd/ZnO/Zn MIM devices for H_2 detection have been reported by Dutta *et al.*[58] The device showed room-temperature H_2 sensing performance. The MIM structure concept can also be extended for measuring the concentrations of gas molecules in capacitive mode.[59] An insulating layer (SiO_2) has been deposited on a Si substrate, and on top of SiO_2, Ta_2O_5 was deposited, which is used as a sensing layer.[59] Au mesh was used as the top electrode and the backside electrodes were attached to silicon.

Thin-film transistors. The concept of field-effect transistors was first introduced by Julius Edgar Lilienfeld in around 1925 for the design of amplifiers, and a few decades later in 1962 the same type of device was demonstrated for gas sensing.[7] Chemiresistor-based TFT devices synthesized through either mechanical or chemical exfoliation, chemical vapor deposition (CVD), or physical evaporation have been employed for VOC, NH_3, at NO_2 detection at the ppm level.[60–62] The problem one encounters during TFT development is silicon-related crystallinity formation, and this problem possibly could be resolved *via* doping with amorphous silicon (aSi:H). However, due to the low electron mobility, which ultimately lowers the response speed, Si:H TFTs are not suitable for sensor design.[62] A few researchers have reported flexibility during TFT development *via* using organic semiconductors with different chemical and physical properties for better sensor design.[63] Organic polymers

as a sensing material in TFT devices showed promising sensing performance in resistive mode. Fig. 6(b) shows optical images of a metal-oxide/graphene composite transistor gas sensor with a channel length of 3 μm, whereas Fig. 6(c) shows the surface morphology of the SnO_2–graphene structure. The drain current (I_{ds}) as a function of the gate voltage (V_g) from oxide–graphene composites, such as SnO_2–graphene, CuO–graphene, and ZnO–graphene, (as shown in Fig. 6(d)) shows asymmetric I_{ds}–V_g characteristics, whereas only pristine graphene showed symmetrical characteristics. The drain current of the oxide–graphene composite was found to be lower compared to pristine graphene possibly due to a reduction in the number of hole majority carriers in p-type graphene after recombination with electrons from the n-type metal oxide. Furthermore, fast response and recovery times of 1.2 s and 1.6 s, respectively, were shown toward H_2 at room temperature.[7] In general, a reducing-type gas acts as an n-type donor agent in the TFT sensor material (n-type), which increases the electron density in the channels and consequently shifts the threshold voltage towards the origin (less positive). The opposite case (when the threshold voltage shifts in a more positive direction) is true following the exposure of the n-type sensing material of a TFT device to an oxidizing gas.[64] In a similar fashion to TFTs, a capacitively controlled field-effect transistor (CCFET) device, where the air-gap technique is utilized for improved sensing performance, is shown in Fig. 6(a).[65] The capacitor structure with an air gap was fabricated along the side of a field-effect transistor. One plate of the capacitor is covered by a gas-sensitive layer and is floating or connected to the gate electrode. The other plate of the capacitor must be connected to the ground potential. Gas sensing *via* such a device occurs either based on a work-function change (due to gas adsorption) of the sensing material or based on the amount of charge storage in the floating electrode.[66] The passivation layer ensures the reliability of the device and the air gap protects it from harsh environments.[66] A TFT gas sensor does not require a heating element as the biasing arrangement is itself sufficient to provide the corresponding activation energy for bond breaking.[65]

The influence of the sensor structure on the gas-sensing performance is tabulated in Table 2. Cerium oxide (CeO_2) porous thick film with a particle size of 100 nm was investigated for oxygen-gas sensing. The sensor showed a fast response within <8 s at 615 °C.[51,52] It is possible that the existence of channels as well as surface accessibility for target gas molecules and subsequent adsorption/desorption, facilitated by the hierarchical porous structure, are the reasons for the excellent sensing performance compared to bulk or solid materials. Basu *et al.* reported porous ZnO-thin-film-based Pd–Ag/ZnO/Zn and Rh/ZnO/Zn MIM (metal–insulator–metal) methane sensors.[67] The results revealed that Pd–Ag/ZnO/Zn offers fast response and recovery times for the detection of 1% methane.[67] The influence of pre-biasing techniques on indium–gallium–zinc oxide (IGZO) TFT devices for NO_2 sensing were studied by Park *et al.*[65] It was observed that the sensing performance improved when the temperature was increased to 90 °C, which could possibly be attributed to the effect of the electric-field-induced chemisorption of NO_2 in the channels of the IGZO TFT.[65] Most TFT-based sensors face the problem of baseline recovery (the return to baseline resistance before gas exposure). The recovery rate of TFT-based sensors can be improved *via* irradiation with UV light at the sensing channel.[60] UV light irradiation results in the removal of oxygen ions from the sensing surface and ensures fewer interactions with gas molecules. It was observed that only a few gas molecules remain in the vicinity of the sensing surface, as such irradiation yields faster removal rates of gas molecules.[68] Furthermore, interdigital capacitive (IDC)

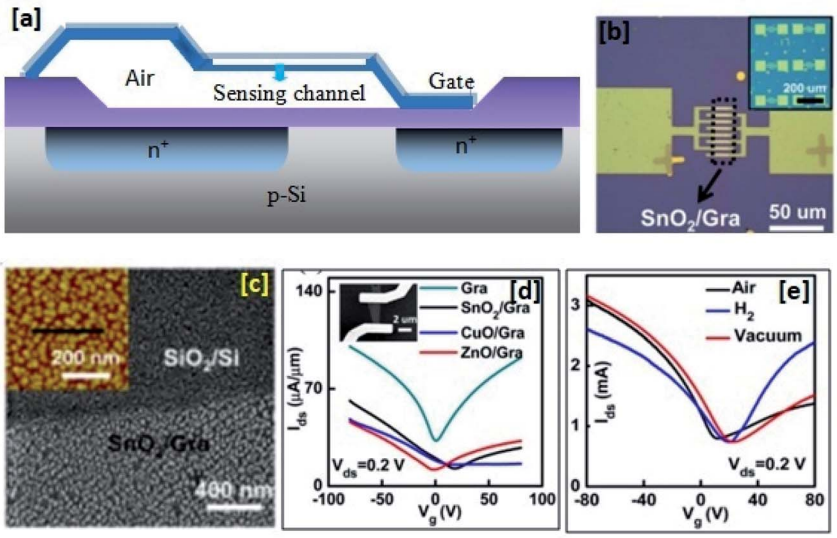

Fig. 6 (a) A schematic view of a CCFET gas sensor (this figure has been reproduced from ref. 66 with permission from Elsevier, copyright 1996). (b) Optical images of a metal-oxide/graphene composite transistor. (c) The AFM surface morphology of SnO_2/graphene. (d) The drain current as a function of the gate voltage from graphene composites with SnO_2, CuO, and ZnO, and (e) the gas-sensing characteristics of an oxide–graphene composite transistor (this figure has been reproduced from ref. 7 with permission from the Royal Society of Chemistry, copyright 2015).

Table 2 The response parameters of metal-oxide-based sensor structures

No.	Structure	Material	[a]Opt temp. (°C)	[b]D. range (ppm)	[c]Res. time (s)	[d]Rec. time (s)	Gas	Stability	[e]Ref.
1	Resistive	Cerium oxide	700	10^5–10^3 Pa	10	NA	O_2	Good	52
		Cerium oxide	615	0.01–1 Pa	11	8	O_2	Excellent	53
		p-TiO_2	320	50	120	<60	Ethanol	Average	21
		Carbon nanotubes	25	0.48–2.34%	90	140	Acetone	Average	53
2	MIS	Pd–SiO_2–Si	667	200	20	40	F144	Poor	54
		Pd–TiO_2–Si	200	0.5–50	7	20	Acetone	Good	48
		Pd–Si_3N_4–SiO_2–Si	150	500	50	150	H_2	Poor	55
		Pd–TiO_2 thin film	50	0.1–2	10	120	H_2	Poor	34
		Pd–Ag/PS/Si/Al	27	0.01–1%	8	207	H_2	High	56
3	MIM	Rh/ZnO/Zn	220	0.01–1%	24.5	72.3	CH_4	Good	67
		Pd–Ag/ZnO/Zn	220	0.01–1%	5.1	16.14	CH_4	Good	67
		Pd/ZnO/Zn	27	2000–20 000	120	840	H_2	Poor	58
		Pd–Ag/ZnO/Zn	150–300	0.01–1%	5.1	16.1	CH_4	Good	57
		TiO_2	23	10–90%	25	65	H_2O	Satisfactory	49
4	TFT	InGaZnO	90	1–20	20	NA	NO_2	NA	65
		WS_2/IGZO	27	1–300	NA	30 min	NO_2	Average	62
		Pentacene	27	0.5–3	70	60	NH_3	Poor	63
5	Capacitive	$CoFe_2O_4$	31	7–100	180	180	Ethanol	NA	69
		Graphene oxide	25	1–70	20	15	Ethanol	Excellent	70
		Al_2O_3	NA	40–98%	10–90	NA	H_2O	NA	71

[a] Opt temp. = optimum temperature. [b] D. range = dynamic range. [c] Res. time = response time. [d] Rec. time = recovery time. [e] Ref. = reference, NA = not applicable.

structures coated with a cobalt ferrite ($CoFe_2O_4$) nanocomposite have been employed for ethanol gas sensing. The device showed a near-room-temperature (31 °C) ethanol response, even at a concentration of 7 ppm, with a response time of 180 s.[69]

Alcohol sensors

The efficient detection of the vapor phases of a wide range of organic molecules, including alcohols, ketones and aromatic hydrocarbons, by means of metal-oxide nanostructure is an extremely important area as far as pollution control is concerned.[70–103] Alcohol consumption can cause driving errors together with traffic-rule violations, potentially leading to death. The inhalation of alcohol may lead to headaches, queasiness, stomach pains, vertigo, nausea, sluggishness, eye irritation, and cerebral pain.[70–85] Therefore, alcohol detection is in high demand to prevent dangerous driving and for food quality monitoring, especially alcoholic beverages.

State-of-the-art alcohol, ketone, and BTX sensing studies are tabulated in Table 3. A comparative study of pure and Au-modified ZnO nanowires for ethanol sensing was carried out by Ramgir *et al.*[72] The results show that the Au-modified sensor films have faster response/recovery times: 5 s and 20 s, respectively. These faster reaction kinetics are attributed to the catalytic activity of Au, as well as nano-Schottky Au–ZnO junction formation.[72] The surface engineering of TiO_2 nanobelts *via* photoreduction through an acid-corrosion procedure for the formation of Ag–TiO_2 heterostructures offered higher sensitivity and selectivity towards ethanol with improved response times. It is believed that the manipulation of the surface roughness and the metal–TiO_2 composite heterostructures were the influencing factors determining the chemical sensitization dynamics based on interfacial charge transfer.[33] The role of porous nanostructures in determining ethanol sensing behaviour was investigated by Yang *et al.*[73] SnO_2/Zn_2SnO_4 hierarchical porous nanospheres were found to offer an optimum response at 250 °C, with a detection limit as low as 0.5 ppm. The lower detection limit of the SnO_2/Zn_2SnO_4 nanospheres can possibly be attributed to the porous structure, as well as heterojunction formation between SnO_2 and Zn_2SnO_4.[73] A room-temperature ethanol study was carried out by Pandeeswari *et al.*[82] and Shao *et al.*[74] As per Shao *et al.*, synergistic effects from the heterojunctions (Au/SnO_2 and C_{60}/SnO_2) and the modulation of potential barriers play crucial roles in enhancing the detection performance.[74]

The facile synthesis of 3 mol% Al-doped NiO nanofibers resulted in a significant increase in methanol response at temperatures from 225 °C to the optimal operating temperature, and the limit of detection became lower as the temperature was increased further.[35] Composites of indium tungsten oxide with different In/W ratios exhibited an ultrafast response to methanol at an optimum temperature of 312 °C. The fastest response time of 2 s and recovery time of 9 s were recorded at a methanol concentration of 200 ppm.[35] The fast response/recovery characteristics are possibly due to the enhanced surface states in the device channels due to majority carrier accumulation around the fully charged grain boundary sites. Three-dimensional effects from nanostructures possibly offer better sensing properties, as was observed in the work of Yang *et al.*[76] In their research, a hematite (α-Fe_2O_3) hollow sphere based sensor offered a low methanol detection limit of 1 ppm and optimal sensing performance at 280 °C.[76] 3D nanostructures with numerous macro/micropores can be an additional advantage in gas sensing. $La_{1-x}Mg_xFeO_3$ 3D macroporous structures with different concentrations of Mg^{2+}

Table 3 Alcohol sensing parameters using different metal-oxide nanostructures

No.	Material	Material synthesis	Vapor	[a]Opt. temp.	[b]D. range (ppm)	[c]RM (%)	[d]Res. time (s)	[e]Rec. time (s)	[f]Ref.
1	ZnO nanowires	Hydrothermal	E	325	5–100	1.33	5	20	72
2	SnO_2 nanorods	Hydrothermal	E	300	10–300	31.4	1	1	77
3	Aloe-like SnO_2	Hydrothermal	E	285	50–1000 ppb	23	1.53	76	78
4	ZnO nanorods	Hydrothermal	E	280	12.5–500	2.5	16	120	79
5	TiO_2 nanobelts	Hydrothermal	E	250	20–500	33.661	1	2	33
6	Zn_2SnO_4 spheres	Hydrothermal	E	250	0.5–100	1.4	2	114	73
7	Er-doped SnO_2	Co-precipitation	E	240	20–750	48	35	40	80
8	CuO nanocrystals	RF sputtering	E	180	12.5–500	2.2	31	52	81
9	TiO_2 thin film	Sol–gel dip	E	30	10–50	14–535	65	20	82
10	Au–SnO_2/C_{60}	Hydrothermal	E	27	0.5–50	16.8	35	9	74
11	SnO_2 thin film	Sol–gel	M	350	2600–100 000	24	NA	NA	61
12	Al-doped NiO	Facile method	M	325	10–500	10.4	199	15	28
13	Ce-doped In_2O_3	Hydrothermal	M	320	35.2–100	35.2	14	10	24
14	$InWO_3$	Hydrothermal	M	312	20–1000	18.1	2	9	75
15	α-Fe_2O_3 spheres	Hydrothermal	M	280	1–100	25.1	8	9	76
16	ZnO/SnO_2	Hydrothermal	M	200	1–300	80	20	65	83
17	$La_{1-x}Mg_xFeO_3$	Template method	M	190	10–300	146.2	17.7	25.4	84
18	SnO_2 spheres	Solvothermal	M	80	5–500	190.88	10	10	85
19	TeO_2 nanowires	Evaporation	P	50	100–1000	3.15	<30	<30	86
20	Hollow CuO fibers	Template method	P	200	1–100	4.66	19.18	63	87
21	$ZnSnO_3$	Facile precipitation	P	200	1–500	10.3	<100	90	88
22	$SmFeO_3$ powders	Decomposition	P	400	0.01–3	11	0.5	3	89
23	Ag/SnO_2 spheres	Chemical route	P	300	50–300	146.02	20	150	90
24	$SrCO_3$/graphene	Cataluminescence	P	245	0.2–32	5.8	2	20	91
25	TiO_2 thick film	Chemical method	P	120	0–5000	60	NA	NA	92
26	Au-α-MoO_3 hollow spheres	Solvothermal	B	250	5–100	1.3	NA	NA	96
			T		0.1–100	2.5	11	57	
			X		0.5–100	5.1	118	289	
27	Cu_2O octahedra	Vapor deposition	B	230	5–200	4.3	3	4	93
28	Au–ZnO	Hydrothermal	B	206	1–200	16.25	5	36	97
			T			46.43	2	50	
			X			76.47	2	24	
29	ZnO nanoflower	CBD	B	200	0.5–700	79.1	15	58	98
			T			85.4	10	50	
			X			87.4	9	38	
30	TiO_2 nanotubes	Anodization	B	150	1–400	25	56.14	152.96	35
			T			21	84.93	128.54	
			X			20	103.80	152.30	
31	Carbon nanotubes	Dispersion	T	27	400–1200	0.001	120	8	99
32	Carbon nanotubes	Chemical method	B	25	33–500	0.7	1.5	2.75	100
			T			1	2.5	1.75	
			X			5	6	4	
33	SnO_2 reduced graphene oxide	Facile hydrothermal	K	27	10–2000	2.19–9.72	300	200	43
34	ZnO nanorods	Aqueous solution	K	300	1–100	30.4	5	15	95
35	$ZnFe_2O_4$ nanospheres	Solvothermal	K	200	11.8–30	42.1	9	272	25
36	ZnO thin film	CVD	K	250–375	1000–2000	45	240	250	101
37	ZnO–SnO_2 nanowires	CVD	K	140–320	0.01–0.2	NA	7	40	94
38	PdAu/SnO_2 nanosheets	Hydro-solvothermal	K	250	1–100	6.5	5	4	102
39	Co_3O_4 nanocubes	One-pot hydrothermal	K	240	10–1000	4.88	2	5	103

[a] Opt temp. = optimum temperature. [b] D. range = dynamic range. [c] RM = response magnitude. [d] Res. time = response time. [e] Rec. time = recovery time. [f] Ref = reference, E = ethanol, M = methanol, P = 2-propanol, B = benzene, T = toluene, X = xylene, K = ketone.

doping reduced the optimum operating temperature to 190 °C, with very good selectivity towards methanol. Possibly, the ordered macro/micropores in the material together with Mg^{2+} doping make this sensor more sensitive and selective towards methanol.[84]

Thermally synthesized single-crystal tetragonal TeO_2 nanowires with a very high surface-to-volume ratio showed 2-propanol detection at 50 °C.[86] The increasing response magnitude trend at lower temperatures is possibly due to a surface-limited reaction mechanism in this temperature range, whereas above a certain temperature (or at higher temperatures), a decreasing trend was found due to a concomitant process involving a decrease in chemisorbed oxygen ions and mass transfer limitations compared to the fast reaction kinetics.[50] Employing cotton fibres as a bio-template in combination with facile solution combustion resulted in hollow CuO fibres with lengths

in the micrometer range, which exhibited excellent sensitivity and reproducibility, and good selectivity toward 2-propanolin at concentrations ranging from 1–100 ppm.[87] The catalytic effect of Ag nanoparticles on SnO_2 hollow spheres played an important role in determining sensor stability and selectivity.[90] A metal-oxide and graphene composite ($SrCO_3$/graphene) exhibited a 2-propanol response 5.8 times higher than that of pure $SrCO_3$.[91]

Benzene, toluene and xylene (BTX) sensors

The aromatic hydrocarbons benzene, toluene, and xylene (BTX) have a carcinogenic nature, and they are by-products in many petrochemical industries, including coal processing and oil refining.[97] BTX easily mixes with air through vehicle exhaust, makeup, glue, and paint emission.[35] Breathing a small amount of BTX may cause abnormalities in the nervous system, leukemia, lymphoma, and blood production issues.[98] Further, monitoring BTX emitted by fruits like oranges in various stages of ripeness can help harvesting to be carried out in good time before spoilage.[35] Template-free solvothermally synthesized hierarchical α-MoO_3 hollow spheres were modified with different amounts of Au nanoparticles to form hybrid nanomaterials for improving the BTX response.[97] The optimum response was found to be significantly higher in Au-loaded α-MoO_3 than in pristine α-MoO_3.[96] Very fast benzene sensing ($\sim$3 s), employing novel concave Cu_2O octahedral nanostructures, has been reported by Wang *et al.*[93] The fast response and recovery times were attributed to the surface area, pore size, and transport mechanism. The surface area of the concave Cu_2O octahedra was as high as 18.9 $m^2\ g^{-1}$. Furthermore, gaps of *ca.* 9 nm between cross-linked nanoparticles possibly facilitate the generation of more active sites for benzene sensing. Electrochemically synthesized titanium dioxide (TiO_2) nanotubes offered BTX sensing at a relatively low temperature of around 150 °C. Studies reveal that benzene generated the highest response, followed by toluene and xylene.[2,8] In particular, for BTX sensing, a high temperature is the prime requirement due to the high-energy bond-breaking. However, near-room-temperature sensing has been observed using some non-metal oxide materials.[99,100] Two such works are included for better comparison.

Ketone sensors

Ketones find widespread applications in pharmaceuticals, nail polish remover, and paints, and they are used as solvents for many complex organic compounds. A room-temperature acetone sensing study, utilizing hybrid SnO_2-reduced graphene oxide thin film, in the concentration range of 10–2000 ppm has been reported by Zhang *et al.*[43] The acetone response was found to be two-times higher than that of pure RGO, which can possibly be attributed to the higher surface area of the 3D porous nanostructure of the RGO sheets and SnO_2 nanoparticles. A sensor with interdigitated electrodes utilizing single crystal hexagonal ZnO nanorods deposited on a Si wafer offered promising acetone sensing performance at 300 °C, with response and recovery times of $\sim$5 s and 15 s, respectively.[95] Such Si-technology-based sensors have flexibility for large-scale production at low cost. A template-free solvothermal route with ethanol/ethylene glycol (EG) as binary solvents was employed to prepare porous $ZnFe_2O_4$ spherical structures.[25] The fabricated sensor offered excellent selectivity toward acetone at an optimum temperature of 200 °C, with a response magnitude of $\sim$11.8. A cataluminescence ketone sensor employing a composite form of SnO_2 : ZnO nanowires coated with Au/reduced-graphene-oxide was developed by Yu *et al.*[94] Their sensor showed an extremely low acetone detection limit down to 0.01 ppm acetone at 140 °C. The possibly catalytic effect of the Au ($\sim$14 nm in size)/reduced graphene oxide composite gives this sensor a fast response with excellent repeatability.[94]

Effects of nanostructure dimensionality

The nanostructure dimension affects the gas sensing performance drastically. Zero-dimensional nanoparticles offer higher numbers of adsorption sites and better catalytic activity, possibly lowering the activation energy required for gas-molecule dissociation.[6,7,18] Smaller particles (<10 nm) accumulate more majority carriers in the sensing channels than bigger particles.[2] Furthermore, a particle size of <10 nm or less than the width of depletion region (w) ensures depletion region overlap, which leads to flat band condition. Under these conditions, no potential barrier is found between the surface and bulk material and the sensitivity is enhanced greatly, as the surface state is dominant. However, the use of such small-sized particles is limited by thermal instability, agglomeration, and film porosity.[2,41] One-dimensional materials, such as nanowires, nanorods, nanoribbons, and nanotubes, offer higher sensitivity compared to conventional materials, such as bulk materials or thin films, under a wide variety of operating conditions. All these nanostructures have radii of 10–100 nm, which are comparable to the width of the depletion region (w), facilitating the easy modulation of the conduction channels.[22] A high surface-to-volume ratio, good surface accessibility, and chemical/thermal stability are possibly the reasons for the better transport qualities. Hollow nanostructures, such as nanocages and nanospheres, are excellent gas-sensing materials, facilitating high permeability with an optimal surface area for gas diffusion. Optimal sensing at the active surface sites results in higher sensitivity with optimum response/recovery characteristics.

Nanostructures with hollow structures are achieved through controlled synthesis, such as layer-by-layer coating, template-free hydrothermal self-assembly, and sacrificial template methods (chemical precipitation or spray pyrolysis).[50] So many techniques, including chemical processes and physical processes, are available to grow off-chip nanostructures. In general, off-chip nanomaterials are first synthesized and then transformed on the heating platform for integration. Integration is done either *via* drop-casting or spin-coating methods. However, such transformations of nanomaterials on the heater may severely affect the intended morphology, reduce the heating area, lead to a loss of sensing surface, or result in poor

electrode bonding with the sensing surface.[50] However, on-chip nanomaterial production on integrated platforms can become complex and necessitates the development of sophisticated techniques to control the growth direction, which possibly leads to better morphology control. Most researchers have employed colloidal spheres as sacrificial templates or carried out the capillary infiltration of a liquid precursor to fabricate hollow spheres or macropores in metal oxide structures, respectively, due to the ease of self-assembly and the high mechanical stability.[50] Such 3D hollow spheres offer three-dimensional interactions with the analysis gases, facilitating rapid sensing with short recovery times *via* maintaining equilibrium between the surface reactions and rates of reactant diffusion.

As far as gas sensing is concerned, key features of nanostructures are as follows. (i) Nanoparticles offer higher surface-to-volume ratios, which facilitate a maximum number of interaction sites compared with nanomaterials with different dimensionality. (ii) One-dimensional electron transport through a minimum number of grain boundaries improves the response/recovery characteristics of sensor devices. (iii) Two-dimensional (2D) nanostructures offer free edge energy to the system, which eventually increases the activation energy for gas adsorption and desorption. (iv) Three-dimensional (3D) nanostructures offer a larger surface area, as well as free surface energy.[20,21,41,45] Table 4 shows the nanostructure dimensionality effects on sensor performance. Sol–gel-derived ZnO nanoparticles showed fast response (2 s) and recovery (20 s) times at 280 °C for NO_2 sensing.[18] A sensor made of spray-pyrolysis-synthesized ZnO nanocrystals on carbon nanotubes (ZnO-CNT) showed linear sensitivity towards methanol gas at 200 °C.[115] Temperature-controlled conductivity and transconductance plays a significant role in the use of this active ZnO-CNT material for sensing gas.[115] Al-doped ZnO ultrathin nanosheets exposed to ethanol offered a response magnitude of 90.2 with a response time/recovery time of 1.6 s/1.8 s at 370 °C. Furthermore, the sensor exhibits a highly repeatable nature, and it is ethanol-selective with long-term stability.[12] Doping-induced intrinsic defects as well as surface energy of the exposed nanosheet planes are possibly the reasons for the excellent sensing properties towards ethanol.[12] The chemical vapor deposition (CVD) of a single SnO_2 nanowire between two metal electrodes has been investigated for ethanol detection.[124] A single nanowire (diameter: 60 nm; length: 3.5 μm) is capable of selectively detecting seven different gases with 94.3% accuracy based on principal component analysis and a machine learning algorithm.[124] The performance of Pd-loaded SnO_2 hollow spheres (obtained *via* an adsorption–calcination process) towards methane showed a response magnitude of 4.88 at 300 °C, with a fast response time/recovery time of 3 s/7 s.[129] Oxygen spillover due to the catalytic effects of Pd and PdO–SnO_2 heterostructures result in better CH_4 sensing performance compared to pristine SnO_2.[129]

Effects of the substrate

On-chip nanostructure growth is difficult and can contaminate other devices on the chip. Contamination can be avoided *via* the (off-chip) growth of nanostructures on one substrate followed by subsequent mechanical manipulation to transfer these nanostructures onto (on-chip) the final substrate (either a micro-hotplate chip or SiO_2/Si) for sensor integration. This type of process has advantages as well as disadvantages.[39] The advantages of such mechanical manipulation can be understood *via* examining the use of single nanowires in TFT devices. The growth of a single nanowire is difficult and costly for use in TFT devices. We can grow multiple nanowires and then easily extract a single nanowire from these and place it in between the source and drain terminals of the FET device to realize a sensing channel.[39] However, the drawback of such a structural transformation, from the original substrate (SiO_2) to the final device substrate (SiO_2/Si), is that this can lead to crystal structure variations. The crystal structure can vary even if only a 1% lattice constant variation occurs along the nanostructure axial direction. Further, there is the possibility that the nanostructure experiences axial tensile or compressive stress on the new substrate due to structural deformations arising from mechanical transformation. Off-chip nanostructures grown and then transformed on-chip are limited when it comes to large-scale production. It is worth mentioning that heterogeneous substrates are preferable for growing 1D nanostructures. In general, one-dimensional growth occurs mostly along the [001] direction.[10] However, the effects of heterogeneous substrates, like Si + W-supported Au film, offer [010] or [100] preferred growth directions.[10]

Roles of electrodes

Sensitivity is inversely proportional to the gap between the two electrodes. Further, the electrode spatial density increases with a reduction of the gap between the electrodes. A comparison of the effect of the electrode gap on the sensor response between two nanostructures, *viz.*, nanowires and nanorod, was made by Wang *et al.*[1] The results suggested that the nanowire-based sensor offered a better response, possibly owing to geometric effects associated with the higher spatial density of the SnO_2 nanowires compared to the SnO_2 nanorods.[1] The catalytic activity of electrodes is an additional advantage when it comes to sensing. Oxygen spillover around catalytic electrodes can enhance the sensitivity and selectivity.[134] The electrode contact can be either ohmic contact or Schottky contact, based on the work function difference ($\Delta\Phi$).[134] A higher work function difference ($\Delta\Phi$) leads to Schottky contact (as shown in Fig. 7), with a higher built-in potential ($q\Phi$) and barrier height (Ψ_b). Ohmic contact is where the barrier height is almost negligible, or it may be reduced to flat-band conditions upon being triggered by gas adsorption. Gas molecules at the electrode sensing material interface lead to dipole accumulation, which possibly is the reason behind carrier tunnelling from thermionic field emission.[134] Fig. 7(a) demonstrates the grain boundaries (a microscopic view of the sensing layer) between two electrodes. The intragrain energy bands are the reason for depletion region formation at the interfaces. However, energy bands at the electrodes and grain interfaces can be characterized based on a work function difference due to dissimilar materials. It is worth mentioning here that intragrain energy-band bending is higher compared to at the electrode–grain interfaces, possibly

Table 4 The performance parameters of sensors based on different dimensional materials

No.	Structure	Material	Method	[a]Temp. (°C)	[b]Conc. (ppm)	Gas	[c]Res. time (s)	[d]Rec. time (s)	[e]Ref.
1	Nanoparticles	ZnO	Brush coating	280	234	NO_2	2	20	18
		ZIF-67 SnO_2 nanoparticles	Chemical	205	5000	CO_2	15	25	104
		Cd_2SnO_4 nanoparticles	Combustion	170		Alcohol	14	280	6
		RGO-decorated ZnO	RF sputtering	150	100	H_2	28	NA	105
		Graphene and SnO_2	CVD	50	100	H_2	1	1	7
		Carbon nanoparticles	Chemical	27	100	CO and H_2	20	>10 min	106
		Ag@UiO-66(Zr)–NO_2	Chemical	27	1	H_2S	200	NA	107
2	Nanorods	Ni-doped SnO_2	Hydrothermal	450	1000	Ethanol	30	600	12
		La_2O_3 nanorods	CBD	450	400	CO_2	80	50	108
		Loaded Pt@SnO_2	Hydrothermal	300	200	Ethanol	2	20	109
		ZnO nanorods	Sputtering	300	200	NO_2	60	80	110
		ZnO nanorods	Hydrothermal	150–250	1–50	NO_2	<120	<150	111
		NiO nanorods-flowers	Solvothermal	200	100	Ethanol	48	40	112
		Co_3O_4 nanorods	Hydrothermal	180	200–1000	Acetone	60	60	113
		ZnO nanorods	Chemical	25	30 000	O_3	100	600	114
3	Nanotubes	ZnO on CNTs	Spray pyrolysis	200	600	Methanol	160	660	115
		CuO nanostructures	Annealing	175	1000	CO	29	37	116
		3D TiO_2/graphene CNTs	CVD	27	500	Toluene	60	90	39
		Pt nanoparticles/CNTs	Chemical bath	27	80	CO	≤30	40	117
		SnO_2/SnS_2 nanotubes	Hydrothermal	27	100	NH_3	21	110	118
4	Nanoplates/nanosheets	Al@ZnO nanosheets	Chemical	370	90.2–100	Ethanol	1.6	1.8	13
		SnS_2 nanoplates	Hydrothermal	27	50	NO_2	NA	NA	119
		Porous CuO nanosheets	Hydrothermal	27	10 ppb	H_2S	234	76	120
		ZnO nanosheets	Template-free	27	100	Acetone	5	28	121
		Graphene nanosheets	Lyophilization	25	10	NO_2	48	3180	122
		CuO nanosheets	Surfactant-free	240	1.2	H_2S	4	9	123
5	Nanowires	SnO_2 nanowires	CVD	400	1–50	Ethanol	2–10	5–14	124
		ZnS nanowires	VLS	320	1	Acetone	7	5	125
		ZnO nanowires	Sol–gel	250	100	CO	60	14	126
		ZnO nanowires	Hydrothermal	225	0.5	NO_2	24	12	127
		SnO_2 nanowires	VLS	200	0.5	NO_2	43	18	40
		Pt/G tellurium	Hydrothermal	27	4000	H_2	6	5.1	128
6	Hollow spheres	SnO_2 hollow spheres	Calcination	300	250	CH_4	3	7	129
		ZnO hollow spheres	Precipitation	300	300	Ethanol	36	35	130
		Porous ZnO/$ZnCO_2O_4$	Solvothermal	275	40	Acetone	4	36	131
7	Nanoflowers	Double-faced ZnO	Solution	270	50–500	NO_2	25–30.8	14.1	8
		ZnO nanoflowers	CBD	200–300	100–0.5	Methanol	48	25	132
		Hierarchical tin oxide	Hydrothermal	200	100	Methanol	4	8	38
		Hierarchical SnO_2	Hydrothermal	27	100	Ethanol	1	2	14
		Hierarchical Cu_2O/CuO	Power method	27	0.001	NO_2	60	140	133

[a] Temp. = optimum temperature. [b] Conc. = concentration. [c] Res. time = response time. [d] Rec. time = recovery time. [e] Ref = reference, NA = not available.

due to the wider depletion width (w) in the intragrain region. Fig. 7(b) shows an enlarged view of an electrode–grain Schottky interface, assuming that a grain is a 3D spherical ball for approximate quantitative understandings. Three-dimensional geometries (ρ, θ, ϕ) have been considered to locate the origin of the grain and the width of depletion region (w) (in air and in the target species). d and w are the grain size and depletion width at the electrode–grain interface, respectively, (note that a depletion region forms only on the grain side) and they are related according to eqn (9).[19,20]

$$w = L_d\sqrt{\frac{eV^2}{kT}} \quad (9)$$

where L_d is the Debye length, V is the surface potential, and k is the Boltzmann constant. However, carrier transport through the electrode-grain region is essentially influenced by the grain size (diameter = d) and the width of the depletion region (w). When $w \leq 2d$, it can be stated that a carrier can transport through the barrier height *via* a neck (channel) control mechanism, where conductivity is determined based on the barrier height difference ($q\Phi_a - q\Phi_w$) and the cross-sectional area of the interface channel (as shown in Fig. 7(b)).[20] To the contrary, smaller grains ($d < 2w$) have a higher SVR and therefore attract more oxygen at the active sites. Oxygen spillover at the grain boundary is accelerated upon accepting electrons from the conduction band, which causes upward band bending. Such bending restricts the flow of charge carriers through the channel, and the conduction mechanism is governed by a grain control mechanism. In the grain control mechanism, a grain is fully depleted and devoid of mobile charge carriers. The bending

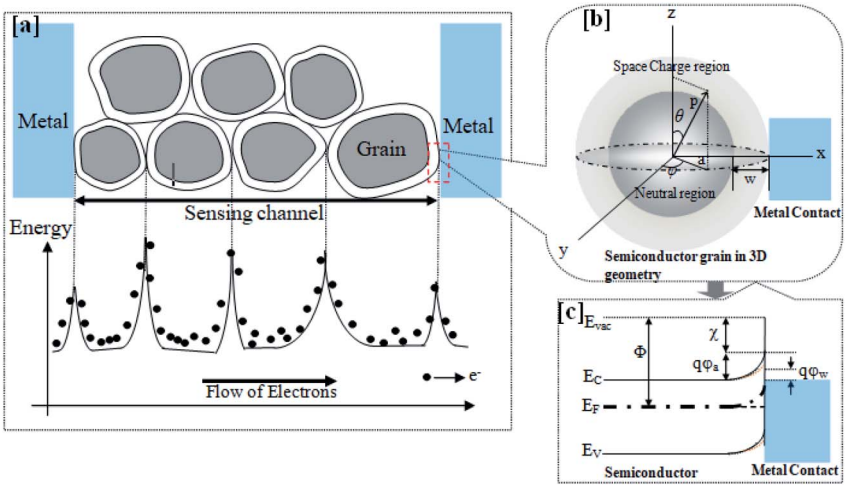

Fig. 7 (a) A diagram of the sensing layer, representing the micro/nanoscopic (not to scale) grain boundaries between two electrodes and the corresponding energy band diagram (two types of energy band, *viz.*, (i) metal–semiconductor (grain) and (ii) intra-semiconductor grain, are shown in the model). (b) An enlarged view of the metal–semiconductor (grain) interface model, assuming grains to be 3D spherical balls for approximate understanding in a quantitative fashion. (c) An energy band diagram of a metal–n-type semiconductor (grain) interface in air and after gas exposure (shown by the dotted brown lines).

height ($q\Phi_a$)/barrier height (Ψ_b) depends on the carrier density (N_d) and depletion width (w) according to eqn (10).[19,20]

$$\Psi_b = q\Phi_a = \left(\frac{N_d e^2}{2\varepsilon_0}\right) w^2 \quad (10)$$

In the case of larger grains ($d \gg 2w$), the conduction mechanism is governed by Schottky barriers at the grain boundaries, which are independent of grain size and almost insensitive to the gas chemisorption process. The conductivity mainly depends on intrinsic charge carriers.[20,23] Platinum (Pt), palladium (Pd), and gold (Au) are the most preferred electrode materials for sensing due to their catalytic activities towards the target species. Pt is preferable over Au because of reliability problems relating to Au.[135] On the other hand, Pd is mostly used for hydrogen sensing due to its easy dissociation to H^+ ions and the subsequent formation of PdH.

Selectivity, repeatability and reliability issues

Metal oxide semiconductors are capable of reacting with a variety of oxidizing and reducing gases. Such nonspecific properties make them less attractive for selective gas sensor design. Further, the realization of high sensitivity towards a specific gas is limited by the absence of a specific functional group with lower electron polarity.[2] Composites between metal oxides and other functional materials are found to offer better selectivity, as reported in many literature studies.[6,80,102] Metal oxides combined with conducting polymers have been used for the last few decades to fabricate selective room-temperature gas sensors. This particular type of structure (metal-oxide semiconductor/polymer) is attractive because of the existence of functional groups within the composite structure.[136] Selectivity improvements *via* embedding a filter on sensor surfaces was an earlier form of technology used to screen certain gases, and it allowed for oxidation and reduction reactions. The principal filtering mechanism was either the adsorption or obstruction of gaseous molecules. In the case of an adsorption process, the filter material is chosen such that it is capable of adsorbing a specific gas and passing it on to react with the sensing surface. On the other hand, a size-dependent filter obstruction mechanism is where relatively larger molecules are obstructed and the intended specifically sized molecules are allowed to react. For example, activated alumina particles and microporous zeolite membrane filters on a metal oxide sensor resulted in enhanced selectivity towards isoprene and formaldehyde, even under humid conditions.[3] However, the need for the frequent replacement of the filter due to contamination and damage by interfering gases makes this approach less popular in practice. Selectivity improvements *via* the principal component analysis of multiple-sensor data can be found in the literature.[137] However, the complexity of these designs, and the cost and size of the final designs make this approach less attractive. Metal oxides alone sometimes are not sufficient for improving sensor response. It has been observed that the uniform incorporation of reduced graphene oxide (RGO) into metal oxide clusters to form hybrid interfaces can offer better performance in terms of the sensor response magnitude and selectivity.[129] RGO introduces oxygen vacancies (V_O), and additional activation energy is generated from the heterostructure interface.[138] The selectivity tuning of metal oxides, employing various (Fe, Cu, Al) foreign elements at different ratios, towards the sensing of a number of gases has been reported by Lupan *et al.*[137] These dispersions of metal particles increase the SVR and change the electronic properties of the surface, facilitating selective gas adsorption.[4] Different weight ratios of Fe, Cu, and Al in ZnO tetrapods not only led to selectivity for different gases but also produced different nanostructure morphologies. The sensor results demonstrated good H_2 sensing using pristine

ZnO tetrapods, whereas the same ZnO tetrapods when modified with Fe or Cu microparticles showed an ethanol-selective nature. Furthermore, on one hand, ZnO tetrapods mixed with a low percentage of Al microparticles (ZnO : Al = 20 : 1) exhibited H_2 sensing capabilities, while on the other hand, a higher percentage of Al (ZnO : Al = 10 : 1) offered methane-selective characteristics.[136] Field-induced channel decoration with discrete nanoparticles (Au, Ag, and Pt) for analyte-specific room-temperature detection has wide versatility. This type of analyte-specific nanoparticle decoration not only enhanced selectivity but also increased sensitivity, even toward sub-parts-per-million gases.[139] It was observed that Au plays a more major role in CO oxidation, Pt is more important in H_2 dissociation, and Ag is more sensitive to C_2H_5OH.[139]

As per the Knudsen equation ($D_K = 4r/3(\sqrt{2RT/\pi M}$), described above), higher weight (M) molecules have a slower diffusion constant (D_K) and, hence, less diffusivity in porous materials.[23] Therefore, gas selectivity can be achieved through controlling the pore sizes of nanostructures. For example, H_2 selectivity (diffusivity and reactivity) has been improved *via* employing porous SnO_2 compared to a non-porous SnO_2 surface.[23] Selectivity improvements of a particular sensing surface can be achieved based on the electron affinity of the target gaseous molecules. According to Zhang *et al.*, lower electron affinity molecules offer higher sensitivity, even at lower activation energies (temperatures).[7] A composite form of SnO_2-graphene showed better H_2 selectivity than for CO and NO, possibly due to the lower electron affinity of H_2.[7]

Repeatability is one of the essential factors for any product to obtain commercial approval. We cannot produce 100% accurate replicates of results between two sensor devices, even if the same fabrication process is followed. There must be a small percentage of dissimilarity between the outcomes from two devices, even if they are taken from the same batch. However, one can efficiently reduce the percentage error drastically *via* adopting careful strategies during the fabrication steps. In addition, synthesis techniques such as spin-coating and dielectrophoretic assembly are found to offer excellent consistency and controllability in outcome, even in terms of device-to-device variations.[63] In most devices, reliability issues are related to the weak attachment of nanostructures to the substrate or changes in the crystallinity of the material. Vertically oriented nanostructures produce tensile stress and strain on a substrate. Therefore, deformation of the substrate crystal structure possibly reduces the robustness of the device. Furthermore, sensor devices become less robust due to environment variations, especially temperature, pressure, humidity, *etc.* The reliability or mechanical robustness of sensor devices can be increased *via* fabrication on flexible substrates.[136] Sensors on flexible substrates offer the possibility for direct synthesis on the substrate, the strong bonding of nanostructures to the substrate, and lower fabrication costs. It is worth mentioning that each sensor device must undergo mechanical reliability testing on curved surfaces (positively bent and negatively bent) before being commercialized.

Conclusions

Gas sensing based on nanostructured metal oxides has been reviewed in the present article. Details relating to gas sensing with special emphasis on (i) sensor device structures (MIM, MIS, resistive, and TFT), (ii) the effects of nanostructure dimensionality, (iii) the role of contact electrodes, and (iv) issues like selectivity, repeatability, and reliability have been investigated critically. The following observations can be made: (a) resistive devices offer a higher sensor response; (b) a fast response can be obtained from vertical devices (MIS and MIM); (c) room temperature sensing is possible with TFT devices; and (d) capacitive sensors are more selective towards specific gases based on the operating frequency. Recovery problems associated with TFT-based room temperature sensing can be accelerated *via* the use of frequent UV illumination or light irradiation. The governing factors for the formation of materials with different dimensionality, including precursors, temperatures, pressures, *etc.*, have also been taken into consideration in detail. The present review could provide very useful guidelines for the science and engineering community to assist them in carrying out research in the field of sensor nanotechnology.

Conflicts of interest

There are no conflicts to declare.

Acknowledgements

This work is supported by TEQIP-III, NIT Jamshedpur, DST India (Project Id-NIT/ECE/RP/2019).

References

1 B. Wang, L. F. Zhu, Y. H. Yang, N. S. Xu and G. W. Yang, Fabrication of a SnO_2 Nanowire Gas Sensor and Sensor Performance for Hydrogen, *J. Phys. Chem. C*, 2008, **112**, 6643–6647.
2 S. Y. Cho, H. W. Yoo, J. Y. Kim, W. B. Jung, M. L. Jin, J. S. Kim, H. J. Jeon and H. T. Jung, High-Resolution p-Type Metal Oxide Semiconductor Nanowire Array as an Ultrasensitive Sensor for Volatile Organic Compounds, *Nano Lett.*, 2016, **16**, 4508–4515.
3 Z. Dai, T. Liang and J. H. Lee, Gas sensors using ordered macroporous oxide nanostructures, *Nanoscale Adv.*, 2019, **1**, 1626–1639.
4 T. A. Dontsova, S. V. Nahirniak and I. M. Astrelin, Metal oxide Nanomaterials and Nanocomposites of Ecological Purpose, *J. Nanomater.*, 2019, **2019**, 5942194–5942224.
5 Y. G. Song, Y. S. Shim, S. Kim, S. D Han, H. G. Moon, M. S. Noh, K. Lee, H. R. Lee, J. S. Kim, B. K. Ju and C. Y. Kang, Downsizing Gas Sensors based on Semiconducting Metal Oxide: Effects of Electrodes on Gas Sensing Properties, *Sens. Actuators, B*, 2017, **248**, 949–956.
6 D. Meena, B. Singh, A. Anand, M. Singh and M. C. Bhatnagar, Phase dependent selectivity shifting behavior of Cd_2SnO_4 nanoparticles based gas sensor

towards volatile organic compounds (VOC) at low operating temperature, *J. Alloys Compd.*, 2020, **820**, 153117–153139.

7 Z. Zhang, X. Zou, L. Xu, L. Liao, W. Liu, J. Ho, X. Xiao, C. Jiang and J. Li, Hydrogen gas sensor based on metal oxide nanoparticles decorated graphene transistor, *Nanoscale*, 2015, **7**, 10078–10084.

8 J. W. Kim, Y. Porte, K. Y. Ko, H. Kim and J. M. Myoung, Micro patternable Double-Faced ZnO Nanoflowers for Flexible Gas Sensor, *ACS Appl. Mater. Interfaces*, 2017, **9**, 32876–32886.

9 R. Jaisutti, M. Lee, J. Kim, S. Choi, T. J. Ha, J. Kim, H. Kim, S. K. Park and Y. H. Kim, Ultrasensitive Room-Temperature Operable Gas Sensors Using p-Type Na: ZnO Nanoflowers for Diabetes Detection, *ACS Appl. Mater. Interfaces*, 2017, **9**, 8796–8804.

10 T. Guo, M. S. Yao, Y. H. Lin and C. W. Nana, A comprehensive review on synthesis methods for transition-metal oxide nanostructures, *CrystEngComm*, 2015, **17**, 3551–3585.

11 V. Inderan, M. M. Arafat, S. Kumar, A. S. M. A. Haseeb, Z. T. Jiang, M. Altarawneh and H. L. Lee, Study of structural properties and defects of Ni-doped SnO_2 nanorods as ethanol gas sensors, *Nanotechnology*, 2017, **28**, 265702–265714.

12 F. Cao, C. Li, M. Li, H. Li, X. Huang and B. Yang, Direct growth of Al-doped ZnO ultrathin nanosheets on electrode for ethanol gas sensor application, *Appl. Surf. Sci.*, 2018, **447**, 173–181.

13 Y. Liu, Y. Jiao, Z. Zhang, F. Qu, A. Umar and X. Wu, Hierarchical SnO_2 Nanostructures Made of Intermingled Ultrathin Nanosheets for Environmental Remediation, Smart Gas Sensor, and Super capacitor Applications, *ACS Appl. Mater. Interfaces*, 2014, **6**, 2174–2184.

14 J. Zhang, S. Wang, M. Xu, Y. Wang, B. Zhu, S. Zhang, W. Huang and S. Wu, Hierarchically Porous ZnO Architectures for Gas Sensor Application, *Cryst. Growth Des.*, 2009, **9**, 3532–3537.

15 X. Xiao, L. Liu, J. Ma, Y. Ren, X. Cheng, Y. Zhu, D. Zhao, A. A. Elzatahry, A. Alghamdi and Y. Deng, Ordered Mesoporous Tin Oxide Semiconductors with Large Pores and Crystallized Walls for High-Performance Gas Sensing, *ACS Appl. Mater. Interfaces*, 2018, **10**, 1871–1880.

16 M. Weber, J. Y. Kim, J. H. Lee, J. H. Kim, I. Iatsunskyi, E. Coy, P. Miele, M. Bechelany and S. S. Kim, Highly efficient hydrogen sensors based on Pd nanoparticles supported on boron nitride coated ZnO nanowires, *J. Mater. Chem. A*, 2019, **7**, 8107–8116.

17 D. Yang, M. K. Fuadi, K. Kang, D. Kim, Z. Li and I. Park, Multiplexed Gas Sensor Based on Heterogeneous Metal Oxide Nanomaterial Array Enabled by Localized Liquid-Phase Reaction, *ACS Appl. Mater. Interfaces*, 2015, **7**, 10152–10161.

18 L. Chandra, R. Dwivedi and V. N. Mishra, Highly sensitive NO_2 sensor using brush-coated ZnO nanoparticles, *Mater. Res. Express*, 2017, **4**, 105030–105043.

19 I. Rawal, Facial synthesis of hexagonal metal oxide nanoparticles for low temperature ammonia gas sensing applications, *RSC Adv.*, 2015, **5**, 4145–4142.

20 B. Bhowmik and P. Bhattacharyya, A Proton Hopping-Guided 3-D Space Charge Model for Quantitative Understanding of Humidity-Dependent Gas Sensing by TiO_2 Nanoflower-Based Devices, *IEEE Trans. Nanotechnol.*, 2017, **16**, 180–188.

21 F. H. Babaei, M. Keshmiri, M. Kakavand and T. Troczynski, A resistive gas sensor based on undoped p-type anatase, *Sens. Actuators, B*, 2005, **110**, 28–35.

22 B. Bhowmik, H. Fecht and P. Bhattacharyya, Vertical Mode Gas Sensing Performance of TiO_2 Nanotube Array by Tuning of Surface Area and Carrier Transport Length, *IEEE Sens. J.*, 2015, **15**, 5919–5926.

23 J. Zhang, Z. Qin, D. Zeng and C. Xiea, Metal-oxide-semiconductor based gas sensors: screening, preparation, and integration, *Phys. Chem. Chem. Phys.*, 2017, **19**, 6313–6329.

24 D. Han, P. Song, S. Zhang, H. Zhang, Q. Xu and Q. Wang, Enhanced methanol gas-sensing performance of Ce-doped In_2O_3 porous nanospheres prepared by hydrothermal method, *Sens. Actuators, B*, 2015, **216**, 488–496.

25 X. Zhou, J. Liu, C. Wang, P. Sun, X. Hu, X. Li, K. Shimanoe, N. Yamazoe and G. Lu, Highly sensitive acetone gas sensor based on porous $ZnFe_2O_4$ nanospheres, *Sens. Actuators, B*, 2015, **206**, 577–583.

26 T. Brezesinski, A. Fischer, K.-ichi Iimura, C. Sanchez, D. Grosso, M. Antonietti and B. M. Smarsly, Generation of Self-Assembled 3D Mesostructured SnO_2 Thin Films with Highly Crystalline Frameworks, *Adv. Funct. Mater.*, 2006, **16**, 1433–1440.

27 J. Zhou, Z. Hua, Z. Liu, W. Wu, Y. Zhu and J. Shi, Direct synthetic strategy of mesoporous ZSM-5 zeolites by using conventional block copolymer templates and the improved catalytic properties, *ACS Catal.*, 2011, **1**, 287–291.

28 C. Feng, Z. Jiang, B. Chen, P. Cheng, Y. Wang and C. Huang, Aluminum-doped NiO nanofibers as chemical sensors for selective and sensitive methanol detection, *Anal. Methods*, 2019, **11**, 575–581.

29 L. Zhu and W. Zeng, Room-temperature gas sensing of ZnO-based gas sensor: a review, *Sens. Actuators, A*, 2017, **267**, 242–261.

30 M. Fernández-Garcia and J. A. Rodriguez, *Metal Oxide Nanoparticles*, Wiley, 2011, DOI: 10.1002/9781119951438.eibc 0331.

31 Z. Dai, T. Lianga and J.-H. Lee, Gas sensors using ordered macroporous oxide nanostructures, *Nanoscale Adv.*, 2019, **1**, 1626–1639.

32 A. Rao, H. Long, A. Harley-Trochimczyk, T. Pham, A. Zettl, C. Carraro and R. Maboudian, In Situ Localized Growth of Ordered Metal Oxide Hollow Sphere Array on Microheater Platform for Sensitive, Ultra-Fast Gas Sensing, *ACS Appl. Mater. Interfaces*, 2017, **9**, 2634–2641.

33 P. Hu, G. Du, W. Zhou, J. Cui, J. Lin, H. Liu, D. Liu, J. Wang and S. Chen, Enhancement of Ethanol Vapor Sensing of

TiO_2 Nanobelts by Surface Engineering, *ACS Appl. Mater. Interfaces*, 2010, **2**, 3263–3269.

34 K. Shubham, R. U. Khan and P. Chakrabarti, TiO_2 Thin Film-based Low Concentration MIS Hydrogen Sensor, *2012 International Conference on Engineering (NUiCONE)*, Ahmedabad, 2012, pp. 1–5.

35 K. Dutta, P. P. Chattopadhyay, C. W. Lu, M. S. Ho and P. Bhattacharyya, A Highly Sensitive BTX Sensor based on Electrochemically Derived Wall Connected TiO_2 Nanotubes, *Appl. Surf. Sci.*, 2015, **354**, 353–361.

36 L. Song, A. Lukianov, D. Butenko, H. Li, J. Zhang, M. Feng, L. Liu, D. Chen and N. I. Klyui, Facile Synthesis of Hierarchical Tin Oxide Nanoflowers with Ultra-High Methanol Gas Sensing at Low Working Temperature, *Nanoscale Res. Lett.*, 2019, 14–24.

37 Y. Seekaew, A. Wisitsoraat, D. Phokharatkuland and C. Wongchoosuk, Room temperature toluene gas sensor based on TiO_2 nanoparticles decorated 3D graphene-carbon nanotube nanostructures, *Sens. Actuators, B*, 2019, **279**, 69–78.

38 Q. H. Wu, J. Li and S. G. Sun, Nano SnO_2 Gas Sensor, *Curr. Nanosci.*, 2010, **6**, 525–538.

39 E. Strelcov, Y. Lilach and A. Kolmakov, Gas Sensor Based on Metal−Insulator Transition in VO2 Nanowire Thermistor, *Nano Lett.*, 2009, **9**, 2322–2326.

40 Y. J. Choi, I. S. Hwang, J. G. Park, K. J. Choi, J. H. Park and J. H. Lee, Novel fabrication of an SnO_2 nanowire gas sensor with high sensitivity, *Nanotechnology*, 2008, **19**, 095508–095512.

41 B. Bhowmik, K. Dutta, A. Hazra and P. Bhattacharyya, Low temperature acetone detection by p-type nano-titania thin film: Equivalent circuit model and sensing mechanism, *Solid-State Electron.*, 2014, **99**, 84–92.

42 B. Bhowmik and P. Bhattacharyya, Highly stable low temperature alcohol sensor based on hydrothermally grown tetragonal titania nanorods, *RSC Adv.*, 2015, **5**, 82159–82168.

43 D. Zhang, A. Liu, H. Chang and B. Xia, Room-temperature high-performance acetone gas sensor based on hydrothermal synthesized SnO_2-reduced graphene oxide hybrid composite, *RSC Adv.*, 2015, **5**, 3016–3022.

44 Z. Wen and L. Tian-mo, Gas sensing properties of SnO_2–TiO_2-based sensor for volatile organic compound gas and its sensing mechanism, *Phys. B*, 2010, **405**, 1345–1348.

45 B. Bhowmik and P. Bhattacharyya, Efficient Gas Sensor Devices Based on Surface Engineered Oxygen Vacancy Controlled TiO_2 Nanosheets, *IEEE Trans. Electron Devices*, 2017, **64**, 2357–2363.

46 J. T. Robinson, F. K. Perkins, E. S. Snow, Z. Wei and P. E. Sheehan, Reduced graphene oxide molecular sensors, *Nano Lett.*, 2008, **8**, 3137–3140.

47 F. Hossein-Babaei and M. Orvatinia, Analysis of thickness dependence of the sensitivity in thin film resistive gas sensors, *Sens. Actuators, B*, 2003, **89**, 256–261.

48 B. Bhowmik, A. Hazra, K. Dutta and P. Bhattacharyya, Nanocrystalline p-TiO_2 based MIS device for efficient acetone detection, *Sensors 2014*, IEEE, Valencia, 2014, pp. 293–296, DOI: 10.1109/ICSENS.2014.6984991.

49 T. Qiang, C. Wang, M. Q. Liu, K. K. Adhikari, J. G. Liang, L. Wang, Y. Li, Y. M. Wu, G. H. Yanga, *et al.*, High-Performance porous MIM-type capacitive humidity sensor realized via inductive coupled plasma and reactive-ion etching, *Sens. Actuators, B*, 2018, **258**, 704–714.

50 A. Rao, H. Long, A. H. Trochimczyk, T. Pham, A. Zettl, C. Carraro and R. Maboudian, In Situ Localized Growth of Ordered Metal Oxide Hollow Sphere Array on Microheater Platform for Sensitive, Ultra-Fast Gas Sensing, *ACS Appl. Mater. Interfaces*, 2017, **9**, 2634–2641.

51 N. Izu, W. Shin and N. Murayama, Fast response of resistive-type oxygen gas sensors based on nano-sized ceria powder, *Sens. Actuators, B*, 2003, **93**, 449–453.

52 N. Izu, W. Shin, N. Murayama and S. Kanzaki, Resistive oxygen gas sensors based on CeO_2 fine powder prepared using mist pyrolysis, *Sens. Actuators, B*, 2002, **87**, 95–98.

53 P. Slobodian, P. Riha, A. Lengalova, P. Svoboda and P. Saha, Multi-wall carbon nanotube networks as potential resistive gas sensors for organic vapor detection, *Carbon*, 2011, **49**, 2499–2507.

54 V. I. Filippov, W. Moritz, A. A. Terentjev, A. A. Vasiliev and S. S. Yakimov, Hydrocarbon and Fluorocarbon Monitoring by MIS Sensors Using an Ni Catalytic Thermodestructor, *IEEE Sens. J.*, 2007, **7**, 192–196.

55 V. G. Litovchenko, T. I. Gorbanyuk, A. A. Efremov, A. A. Evtukh and D. Schipanski, Investigation of MIS gas sensitive structures with Pd and Pd/Cu metal layers, *Sens. Actuators, A*, 1999, **74**, 233–236.

56 J. Kanungo, H. Saha and S. Basu, Room temperature metal insulator semiconductor (MIS) hydrogen sensors based on chemically surface modified porous silicon, *Sens. Actuators, B*, 2009, **140**, 65–72.

57 P. Bhattacharyya, P. K. Basu and S. Basu, Methane Detection By Nano ZnO Based MIM Sensor Devices, *Sens. Transducers J.*, 2011, **10**, 121–130.

58 A. Dutta and S. Basu, Modified metal-insulator-metal (MIM) hydrogen gas sensors based on zinc oxide, *J. Mater. Sci.: Mater. Electron.*, 1995, **6**, 415–418.

59 C. Zamania, K. Shimanoe and N. Yamazoe, A new capacitive-type NO_2 gas sensor combining an MIS with a solid electrolyte, *Sens. Actuators, B*, 2005, **109**, 216–220.

60 T. Pham, G. Li, E. Bekyarova, M. E. Itkisand and A. Mulchandani, MoS_2-Based Optoelectronic Gas Sensor with Sub-parts-per-billion Limit of NO_2 Gas Detection, *ACS Nano*, 2019, **13**, 3196–3205.

61 A. Teeramongkonrasmee and M. Sriyudthsak, Methanol and ammonia sensing characteristics of sol–gel derived thin film gas sensor, *Sens. Actuators, B*, 2000, **66**, 256–259.

62 E. Fortunato, P. Barquinha, A. Pimentel, A. Gonçalves, A. Marques, L. Pereira and R. Martins, Recent advances in ZnO transparent thin film transistors, *Thin Solid Films*, 2005, **487**, 205–211.

63 H. W. Zan, M. Z. Dai, T. Y. Hsu, H. C. Lin, H. F. Meng and Y. S. Yang, Porous Organic TFTs for the Applications on

Real-Time and Sensitive Gas Sensors, *IEEE Electron Device Lett.*, 2011, **32**, 1143–1145.

64 G. Lu, S. Park, K. Yu, Y. S. Ruoff, L. E. Ocola, D. Rosenmann and J. Chen, Toward Practical Gas Sensing with Highly Reduced Graphene Oxide: A New Signal Processing Method To Circumvent Run-to-Run and Device-to-Device Variations, *ACS Nano*, 2011, **5**, 1154–1164.

65 M. J. Park, H. S. Jeong, H. J. Joo, H. Y. Jeong, S. H. Song and H. I. Kwon, Improvement of NO_2 gas-sensing properties in InGaZnO thin-film transistors by a pre-biasing measurement method, *Semicond. Sci. Technol.*, 2019, **34**, 065010–065020.

66 Z. Gergintschew, P. Kometzky and D. Schipanski, The capacitively controlled field effect transistor (CCFET) as a new low power gas sensor, *Sens. Actuators, B*, 1996, **36**, 285–289.

67 P. K. Basu, P. Bhattacharyya, N. Saha, H. Saha and S. Basu, The superior performance of the electrochemically grown ZnO thin films as methane sensor, *Sens. Actuators, B*, 2008, **133**, 357–363.

68 R. Kumar, N. Goel and M. Kumar, UV-Activated MoS_2 Based Fast and Reversible NO_2 Sensor at Room Temperature, *ACS Sens.*, 2017, **2**, 1744–1752.

69 J. Paul and J. Philip, Inter-digital capacitive ethanol sensor coated with cobalt ferrite nanocomposite as gas sensing material, *Mater. Today: Proc.*, 2020, **25**, 148–150.

70 N. L. Teradal, S. Marx, A. Morag and R. Jelinek, Porous graphene oxide chemi-capacitor vapor sensor array, *J. Mater. Chem. C*, 2017, **5**, 1128–1135.

71 R. K. Nahar and V. K. Khanna, A study of capacitance and resistance characteristics of an Al_2O_3 humidity sensor, *Int. J. Electron.*, 1982, **52**, 557–567.

72 N. S. Ramgir, M. Kaur, P. K. Sharma, N. Datta, S. Kailasaganapathi, S. Bhattacharya, A. K. Debnath, D. K. Aswal and S. K. Gupta, Ethanol sensing properties of pure and Au modified ZnO nanowires, *Sens. Actuators, B*, 2013, **187**, 313–318.

73 X. Yang, H. Li, T. Li, Z. Li, W. Wu, C. Zhou, P. Sun, F. Liu, *et al.*, Highly efficient ethanol gas sensor based on hierarchical SnO_2/Zn_2SnO_4 porous spheres, *Sens. Actuators, B*, 2019, **282**, 339–346.

74 S. Shao, W. Wang, Y. Chen, Y. Wang and R. Koehn, Ultrasensitive room-temperature ethanol detection based on Au functionalized nanoporous $SnO_2/C_{60}/SnO_2$ composites, *RSC Adv.*, 2017, **7**, 53925–53931.

75 C. Wang, X. Kou, N. Xie, L. Guo, Y. Sun, X. Chuai, J. Ma, P. Sun, Y. Wang and G. Lu, Detection of Methanol with Fast Response by Mono dispersed Indium Tungsten Oxide Ellipsoidal Nanospheres, *ACS Sens.*, 2017, **2**, 648–654.

76 H. M. Yang, S. Y. Ma, G. J. Yang, W. X. Jin, T. T. Wang, X. H. Jiang and W. Q. Li, High sensitive and low concentration detection of methanol gas sensor based on one-step synthesis αFe_2O_3 hollow spheres, *Mater. Lett.*, 2016, **169**, 73–76.

77 Y. J. Chen, X. Y. Xue, Y. G. Wang and T. H. Wang, Synthesis and ethanol sensing characteristics of single crystalline SnO_2 nanorods, *Appl. Phys. Lett.*, 2005, **87**, 233503–233506.

78 L. Mei, J. Deng, X. Yin, M. Zhang, Q. Li, E. Zhang, Z. Xu, L. Chen and T. Wang, Ultrasensitive ethanol sensor based on 3D aloe-like SnO_2, *Sens. Actuators, B*, 2012, **166–167**, 7–11.

79 M. Z. Ahmad, A. Z. Sadek, K. Latham, J. Kita, R. Moos and W. Wlodarski, Chemically synthesized one-dimensional zinc oxide nanorods for ethanol sensing, *Sens. Actuators, B*, 2013, **187**, 295–300.

80 G. Singh, Virpal and R. C. Singh, Highly sensitive gas sensor based on Er-doped SnO_2 nanostructures and its temperature dependent selectivity towards hydrogen and ethanol, *Sens. Actuators, B*, 2019, **282**, 373–383.

81 A. S. Zoolfakar, M. Z. Ahmad, R. A. Rani, J. Z. Ou, S. Balendhran, S. Zhuiykov, K. Latham, W. Wlodarski and K. Kalantar-Zadeh, Nanostructured copper oxides as ethanol vapour sensors, *Sens. Actuators, B*, 2013, **185**, 620–627.

82 R. Pandeeswari, R. K. Karnand and B. G. Jeyaprakash, Ethanol sensing behaviour of sol–gel dip-coated TiO_2 thin films, *Sens. Actuators, B*, 2014, **194**, 470–477.

83 R. Peng, J. Chen, D. Li, L. Chen and L. Ci, Investigation of the gas-sensitive properties for methanol detection based on ZnO/SnO_2 heterostructure, *IOP Conf. Ser.: Mater. Sci. Eng.*, 2018, **392**, 032016–032020.

84 J. Qin, Z. Cui, X. Yang, S. Zhu, Z. Li and Y. Liang, Three-dimensionally ordered macro porous $La_{1-x}Mg_xFeO_3$ as high performance gas sensor to methanol, *J. Alloys Compd.*, 2015, **635**, 194–202.

85 Y. Li, D. Deng, N. Chen, X. Xing, X. Xiao and Y. Wang, Enhanced methanol sensing properties of SnO_2 microspheres in a composite with Pt nanoparticles, *RSC Adv.*, 2016, **6**, 83870–83879.

86 Y. Shen, A. Fan, D. Wei, S. Gao, W. Liu, C. Han and B. Cui, A low-temperature n-propanol gas sensor based on TeO_2 nanowires as the sensing layer, *RSC Adv.*, 2015, **5**, 29126–29130.

87 C. Dong, X. Xing, N. Chen, X. Liu and Y. Wang, Biomorphic synthesis of hollow CuOfibers for low-ppm-level n-propanol detection via a facile solution combustion method, *Sens. Actuators, B*, 2016, **230**, 1–8.

88 Y. Yin, Y. Shen, P. Zhou, R. Lu, A. Li, S. Zhao, W. Liu, D. Wei and K. Wei, Fabrication, characterization and n-propanol sensing properties of perovskite-type $ZnSnO_3$ nanospheres based gas sensor, *Appl. Surf. Sci.*, 2020, **509**, DOI: 10.1016/j.apsusc.2020.145335.

89 M. Mori, Y. Itagaki, J. Iseda, Y. Sadaoka, T. Ueda, H. Mitsuhashi and M. Nakatani, Influence of VOC structures on sensing property of $SmFeO_3$ semiconductive gas sensor, *Sens. Actuators, B*, 2014, **202**, 873–877.

90 M. Li, H. Zhu, B. Wang, J. Cheng, W. Yan, S. Xia and Z. Tang, Ultrasensitive and highly selective detection of methoxy propanol based on Ag-decorated SnO_2 hollow nanospheres, *Sens. Actuators, B*, 2016, **232**, 545–556.

91 Q. Zhang, F. Meng, L. Zha, X. Wang and G. Zhang, A sensitive cataluminescence-based sensor using a $SrCO_3$/graphene composite for n-propanol, *RSC Adv.*, 2015, **5**, 57482–57489.

92 A. K. Vishwakarma and L. Yadav, Detection of propanol gas using titanium dioxide based thick film, *IOP Conf. Ser.: Mater. Sci. Eng.*, 2018, **404**, 012020–012024.

93 L. Wang, R. Zhang, T. Zhou, Z. Lou, J. Deng and T. Zhang, Concave Cu_2O octahedral nanoparticles as an advanced sensing material for benzene (C_6H_6) and nitrogen dioxide (NO_2) detection, *Sens. Actuators, B*, 2016, **223**, 311–317.

94 L. Yu, H. Song, Y. Tang, L. Zhang and Y. Lv, Controllable deposition of ZnO-doped SnO_2 nanowires on Au/graphene and their application in cataluminescence sensing for alcohols and ketones, *Sens. Actuators, B*, 2014, **203**, 726–735.

95 Y. Zeng, T. Zhang, M. Yuan, M. Kang, G. Lu, R. Wang, H. Fan, Y. He and H. Yang, Growth and selective acetone detection based on ZnO nanorod arrays, *Sens. Actuators, B*, 2009, **143**, 93–98.

96 L. Sui, X. Zhang, X. Cheng, P. Wang, Y. Xu, S. Gao, H. Zhao and L. Huo, Au-loaded hierarchical MoO_3 hollow spheres with enhanced gas sensing performance for the detection of BTX (benzene, toluene and xylene) and the sensing mechanism, *ACS Appl. Mater. Interfaces*, 2017, **9**, 1661–1670.

97 Z. Shen, X. Zhang, X. Ma, R. Mi, Y. Chen and S. Ruan, The significant improvement for BTX sensing performance based on Au-decorated hierarchical ZnO porous rose-like architectures, *Sens. Actuators, B*, 2018, **262**, 86–94.

98 D. Acharyya and P. Bhattacharyya, An efficient BTX sensor based on ZnO nanoflowers grown by CBD method, *Solid-State Electron.*, 2015, **106**, 18–26.

99 A. Ndiaye, P. Bonnet, A. Pauly, M. Dubois, J. Brunet, C. Varenne, K. Guerin and B. Lauron, Noncovalent Functionalization of Single-Wall Carbon Nanotubes for the Elaboration of Gas Sensor Dedicated to BTX Type Gases: The Case of Toluene, *J. Phys. Chem. C*, 2013, **117**, 20217–20228.

100 A. Pauly, J. Brunet, C. Varenne and A. L. Ndiaye, Insight in the interaction mechanisms between functionalized CNTs and BTX vapors in gas sensors: are the functional peripheral groups the key for selectivity?, *Sens. Actuators, B*, 2019, **298**, 126768–126778.

101 P. P. Sahay, Zinc oxide thin film gas sensor for detection of acetone, *J. Mater. Sci.*, 2005, **40**, 4383–4385.

102 G. Li, Z. Cheng, Q. Xiang, L. Yan, X. Wang and J. Xu, Bimetal Pd Au decorated SnO_2 nanosheets based gas sensor with temperature-dependent dual selectivity for detecting formaldehyde and acetone, *Sens. Actuators, B*, 2019, **283**, 590–601.

103 T. Zhoua, T. Zhang, J. Deng, R. Zhang, Z. Lou and L. Wang, P-type Co_3O_4 nanomaterials-based gas sensor: preparation and acetone sensing performance, *Sens. Actuators, B*, 2017, **242**, 369–377.

104 M. E. DMello, N. G. Sundaram and S. B. Kalidindi, Assembly of ZIF-67 Metal–Organic Framework over Tin Oxide Nanoparticles for Synergistic Chemiresistive CO_2 Gas Sensing, *Chem.–Eur. J.*, 2018, **24**, 9220–9223.

105 V. S. Bhati, S. Ranwa, S. Rajamani, K. Kumari, R. Raliya, P. Biswas and M. Kumar, Improved sensitivity with low limit of detection of hydrogen gas sensor based on rGO loaded Ni doped ZnO nanostructures, *ACS Appl. Mater. Interfaces*, 2018, **10**, 11116–11124.

106 D. Kim, P. V. Pikhitsa, H. Yang and M. Choi, Room temperature CO and H_2 sensing with carbon nanoparticles, *Nanotechnology*, 2011, **22**, 485501–485508.

107 S. G. Surya, S. Bhanoth, S. M. Majhi, Y. D. More, V. M. Teja and K. N. Chappanda, A silver nanoparticle-anchored UiO-66(Zr) metal–organic framework (MOF)-based capacitive H_2S gas sensor, *CrystEngComm*, 2019, **21**, 7303–7312.

108 A. A. Yadav, A. C. Lokhande, J. H. Kim and C. D. Lokhande, Enhanced sensitivity and selectivity of CO_2 gas sensor based on modified La2O3 nanorods, *J. Alloys Compd.*, 2017, **723**, 880–886.

109 X. Xue, Z. Chen, C. Ma, L. Xing, Y. Chen, Y. Wang and T. Wang, One-Step Synthesis and Gas-Sensing Characteristics of Uniformly Loaded Pt@SnO_2Nanorods, *J. Phys. Chem. C*, 2010, **114**, 3968–3972.

110 G. J. Sun, J. K. Lee, S. Choi, W. I. Lee, H. W. Kim and C. Lee, Selective oxidizing gas sensing and dominant sensing mechanism of n-CaO-decorated n-ZnO nanorod sensors, *ACS Appl. Mater. Interfaces*, 2017, **9**, 9975–9985.

111 X. Wang, F. Sun, Y. Duan, Z. Yin, W. Luo, Y. A. Huang and J. Chen, Highly sensitive, temperature-dependent gas sensor based on hierarchical ZnO nanorod arrays, *J. Mater. Chem. C*, 2015, **3**, 11397–11405.

112 C. Wang, X. Cui, J. Liu, X. Zhou, X. Cheng, P. Sun, X. Hu, X. Li, J. Zheng and G. Lu, The Design of Superior Ethanol Gas Sensor Based on the Al-Doped NiO Nanorod-Flowers, *ACS Sens.*, 2016, **1**, 131–136.

113 H. Nguyen and S. A. El-Safty, Meso- and Macroporous Co_3O_4 Nanorods for Effective VOC Gas Sensors, *J. Phys. Chem. C*, 2011, **115**, 8466–8474.

114 B. S. Kang, Y. W. Heo, L. C. Tien, D. P. Norton, F. Ren, B. P. Gila and S. J. Pearton, Hydrogen and ozone gas sensing using multiple ZnO nanorods, *Appl. Phys. A*, 2005, **80**, 1029–1032.

115 A. Ayeshamariam, D. Saravanakkumar, M. Kashif, S. Sivaranjani and B. Ravikumar, Analysis on the effect of ZnO on Carbon nanotube by spray pyrolysis method, *Mechanics of Advanced Materials and Modern Processes*, 2016, **2**, 3.

116 L. Hou, C. Zhang, L. Li, C. Du, X. Li, X. F. Kang and W. Chen, CO Gas Sensors based on p-type CuO Nanotubes and CuONanocubes: Morphology and Surface Structure Effects on the Sensing Performance, *Talanta*, 2018, **188**, 41–49.

117 M. Han, J. K. Kim, G. S. Lee, S. W. Kang and D. Jung, A CO gas sensor based on Pt-loaded carbon nanotube sheets, *Jpn. J. Appl. Phys.*, 2019, **58**, SDDE03–SDDE08.

118 R. Li, K. Jiang, S. Chen, Z. Lou, T. Huang, D. Chen and G. Shen, SnO_2/SnS_2 nanotubes for flexible room temperature NH_3 gas sensor, *RSC Adv.*, 2017, **7**, 52503–52509.

119 Z. Yang, C. Su, S. Wang, Y. Han, X. Chen, S. Xu, Z. Zhou, N. Hu, Y. Su and M. Zeng, Highly sensitive NO_2 gas sensors based on hexagonal SnS_2 nanoplates operating at

room temperature, *Nanotechnology*, 2019, **31**, 075501–075530.

120 Z. Li, N. Wang, Z. Lin, J. Wang, W. Liu, K. Sun, Y. Q. Fu and Z. Wang, Room-temperature high performance H_2S sensor based on porous CuO nanosheets prepared by hydrothermal method, *ACS Appl. Mater. Interfaces*, 2016, **8**, 20962–20968.

121 J. Li, H. Fan and X. Jia, Multilayered ZnO Nanosheets with 3D Porous Architectures: Synthesis and Gas Sensing Application, *J. Phys. Chem. C*, 2010, **114**, 14684–14691.

122 Z. Chen, J. Wang, A. Umar, Y. Wang, H. Li and G. Zhou, Three-Dimensional Crumpled Graphene-Based Nanosheets with Ultrahigh NO_2 Gas Sensibility, *ACS Appl. Mater. Interfaces*, 2017, **9**, 11819–11827.

123 F. Zhang, A. Zhu, Y. Luo, Y. Tian, J. Yang and Y. Qin, CuO Nanosheets for Sensitive and Selective Determination of H_2S with High Recovery Ability, *J. Phys. Chem. C*, 2010, **114**, 19214–19219.

124 M. Tonezzer, Selective gas sensor based on one single SnO_2 nanowire, *Sens. Actuators, B*, 2019, **288**, 53–59.

125 X. Wang, Z. Xie, H. Huang, Z. Liu, D. Chen and G. Shen, Gas sensors, thermistor and photodetector based on ZnS nanowires, *J. Mater. Chem.*, 2012, **22**, 6845–6850.

126 M. Sinha, R. Mahapatra, B. Mondal, T. Maruyama and R. Ghosh, Ultra-fast and Reversible Gas Sensing Properties Of ZnO Nanowire Arrays Grown By Hydrothermal Technique, *J. Phys. Chem. C*, 2016, **120**, 3019–3025.

127 M. W. Ahn, K. S. Park, J. H. Heo, J. G. Park, D. W. Kim, K. J. Choi, J. H. Lee and S. H. Hong, Gas sensing properties of defect-controlled ZnO-nanowire gas sensor, *Appl. Phys. Lett.*, 2008, **93**, 263103–263106.

128 T. Y. Hwang, G. M. Go, S. Park, J. Lee, Y. Song, S. Kim, H. B. Cho and Y. H. Choa, Pt/graphene Catalyst and Tellurium Nanowire-based Thermochemical Hydrogen (TCH) Sensor Operating at Room Temperature in Wet Air, *ACS Appl. Mater. Interfaces*, 2019, **11**, 47015–47024.

129 L. Yang, Z. Wang, X. Zhou, X. Wu, N. Han and Y. Chen, Synthesis of Pd-loaded mesoporous SnO_2 hollow spheres for highly sensitive and stable Methane gas sensors, *RSC Adv.*, 2018, **8**, 24268–24275.

130 L. Ge, X. Jing, J. Wang, J. Wang, S. Jamil, Q. Liu, F. Liuand and M. Zhang, Trisodium citrate assisted synthesis of ZnO hollow spheres via a facile precipitation route and their application as gas sensor, *J. Mater. Chem.*, 2011, **21**, 10750–10754.

131 X. Zhou, W. Feng, C. Wang, X. Hu, X. Li, P. Sun, K. Shimanoe, N. Yamazoe and G. Lu, Porous ZnO/$ZnCo_2O_4$ hollow spheres: synthesis, characterization, and applications in gas sensing, *J. Mater. Chem. A*, 2014, **2**, 17683–17690.

132 D. Acharyya, N. Banerjee and P. Bhattacharyya, A comparative study on methanol sensing performance of ZnO nanoflower and nanorod based resistive devices, *Sensors 2014*, IEEE, Valencia, 2014, pp. 811–814, DOI: 10.1109/ICSENS.2014.6985123.

133 J. Hu, C. Zou, Y. Su, M. Li, Y. Han, E. S. W. Kong, Z. Yang and Y. Zhang, Ultrasensitive NO_2 gas sensor based on hierarchical Cu_2O/CuOmesocrystals nanoflower, *J. Mater. Chem. A*, 2018, **6**, 17120–17131.

134 S. P. Lee, Electrodes for Semiconductor Gas Sensors, *Sensors*, 2017, **17**, 683–702.

135 S. Capone, P. Siciliano, F. Quaranta, R. Rella, M. Epifani and L. Vasanelli, Moisture influence and geometry effect of Au and Pt electrodes on CO sensing response of SnO_2 microsensors based on sol-gel thin film, *Sens. Actuators, B*, 2001, **77**, 503–511.

136 Z. Wang, T. Han, T. Fei, S. Liu and T. Zhang, Investigation of Microstructure Effect on NO_2 Sensors Based on SnO_2 Nanoparticles/Reduced Graphene Oxide Hybrids, *ACS Appl. Mater. Interfaces*, 2018, **10**, 41773–41783.

137 O. Lupan, V. Postica, J. Gröttrup, A. K. Mishra, N. H. Leeuw, J. F. C. Carreira, J. Rodrigues, N. B. Sedrine, M. R. Correia, T. Monteiro, *et al.*, Hybridization of Zinc Oxide Tetrapods for Selective Gas Sensing Applications, *ACS Appl. Mater. Interfaces*, 2017, **9**, 4084–4099.

138 M. Frietsch, F. Zudock, J. Goschnick and M. Bruns, CuO catalytic membrane as selectivity trimmer for metal oxide gas sensors, *Sens. Actuators, B*, 2000, **65**, 379–381.

139 X. Zou, J. Wang, X. Liu, C. Wang, Y. Jiang, Y. Wang, X. Xiao, J. C. Ho, *et al.*, Rational Design of Sub-Parts per Million Specific Gas Sensors Array Based on Metal Nanoparticles Decorated Nanowire Enhancement-Mode Transistors, *Nano Lett.*, 2013, **13**, 3287–3292.